3D Printed Heat Pipe Structures Use Application for Thermal Management on Power Dense Small Satellite Platforms

by

Antonio Rodulfo Acuña

A Thesis Presented in Partial Fulfillment
of the Requirements for the Degree
Master of Science

Approved June 2022 by the
Graduate Supervisory Committee:

Jnaneshwar Das, Co-Chair
Patrick Phelan, Co-Chair
Marc Mignolet

ARIZONA STATE UNIVERSITY

August 2022

ABSTRACT

The technology and science capabilities of SmallSats continue to grow with the increase of capabilities in commercial off the shelf components. However, the maturation of SmallSat hardware has also led to an increase in component power consumption, this poses an issue with using traditional passive thermal management systems (radiators, thermal straps, etc.) to regulate high-power components. High power output becomes limited in order to maintain components within their allowable temperature ranges. The aim of this study is to explore new methods of using additive manufacturing to enable the usage of heat pipe structures on SmallSat platforms up to 3U's in size. This analysis shows that these novel structures can increase the capabilities of SmallSat platforms by allowing for larger in-use heat loads from a nominal power density of 4.7×10^3 W/m^3 to a higher 1.0×10^4 W/m^3 , an order of magnitude increase. In addition, the mechanical properties of the SmallSat structure are also explored to characterize effects to the mechanical integrity of the spacecraft. The results show that the advent of heat pipe integration to the structures of SmallSats will lead to an increase in thermal management capabilities compared to the current state-of-the-art systems, while not reducing the structural integrity of the spacecraft. In turn, this will lead to larger science and technology capabilities for a field that is growing in both the education and private sectors.

ACKNOWLEDGMENTS

I would like to thank my advisors, Prof. Patrick Phelan, and Prof. Jnaneshwar Das, for their help and guidance over the past few years. I also want to extend these thanks to Prof. Marc Mignolet for being another member of my committee and providing just as much support. I would also like to recognize the support and patience I received from all my friends and peers, especially Jonathan Gamaunt, Sarah Rogers, and Zoltan Farkas. This would also not be doable without the flexibility offered to me by my employers to even disappear at times to complete this degree; thank you. Finally, I want to thank my family for their immense support throughout graduate school.

TABLE OF CONTENTS

Page

LIST OF TABLES v

LIST OF FIGURES vi

NOMENCLATURE viii

CHAPTER

1 INTRODUCTION 1

1.1 Objectives 2

1.2 3U CubeSat Overview 3

1.3 Heat Pipes 5

1.4 Current Design 7

2 THERMAL ANALYSIS 15

2.1 FEM setup – Heat Pipe Structure 24

2.2 Simulation Results – Heat Pipe Structure 25

2.3 Nominal Orbit Environment 28

2.4 FEM Setup – Entire CubeSat Structure 30

2.5 Simulation Results – Entire CubeSat Structure, Steady State 31

2.6 Simulation Results – Entire CubeSat Structure, Transient 32

3 STRUCTURAL ANALYSIS 34

3.1 FEM Setup 38

3.2 Simulation Results 41

3.3 Stress Evaluation 50

CHAPTER Page

4 TECHNOLOGY IMPACT 56

5 CONCLUSIONS 57

REFERENCES 61

LIST OF TABLES

Table		Page
1.1	Nominal Operating Temperatures of Phoenix CubeSat	4
1.2	Hypothetical Overpowered Temperatures of Phoenix CubeSat	4
1.3	Thermal Mechanical Properties of AlSi10Mg	10
1.4	Thermal Mechanical Properties of Acetone	11
1.5	Thermal Resistance Network of Heat Pipe Connections	15
2.1	Tabulated Spacecraft Radiator Properties	20
2.2	Heat Pipe Structure Alone, Simulation Results	27
2.3	Simulation Orbit Parameters	28
2.4	Entire Structure Steady State Results	32
2.5	Entire Structure Transient Results	33
3.1	In-plane Vibration Environment	34
3.2	Out-of-plane Vibration Environment	35
3.3	Mechanical Properties of AlSi10Mg	36
3.4	Total FEM Element Breakdown	40
3.5	Major Modes of Structure	41
3.6	Largest Sine Sweep Response Values	49
3.7	Largest Random Response PSD Values	50
3.8	Max Stresses Random Response	52
3.9	Factors of Safety, Random Vibration Load	52
3.10	Max Stresses Sine Sweep Response	54
3.11	Factors of Safety, Sine Sweep Load	54

LIST OF FIGURES

Figure Page

1.1 Assembled Phoenix CubeSat 3

1.2 Closed Loop Heat Pipe Diagram 6

1.3 Cross-sectioned Views of Current Heat Pipe Structure 7

1.4 Printed and Tested Heat Pipe, Chao Chang 8

1.5 Versatility of 3D Printed Heat Pipe Structure 9

1.6 Thermal Interface Connection of Heat Pipe Condenser 14

2.1 Simulation Convergence Criteria 16

2.2 Heat Flow Map of Entire CubeSat System 17

2.3 Thermal Resistance Network From Evaporator to Radiator 18

2.4 Radiator Temperature vs. Displacement Comparison 21

2.5 Thermal Resistance Network From Nominal Board to Structure 22

2.6 Heat Pipe Structure FEM 25

2.7 Standalone Heat Pipe Structure – SIM Setup 26

2.8 Standalone Heat Pipe Structure – SIM Results 27

2.9 Simulation Orbit Visualization 29

2.10 Entire Thermal Structure FEM 30

2.11 Entire Structure FEM Results 31

2.12 Entire Structure Transient Temperatures 33

3.1 Entire CubeSat Structure 37

3.2 Entire CubeSat Structure FEM 39

3.3 Visualization of 1D Bolted Region 39

Figure Page

3.4 Deformation Results of Primary Modes 42

3.5 Major Mode on Heat Pipe, 632.96 Hz 43

3.6 Location of Accelerometers 44

3.7 Response Curves From In-plane Sine Sweep, Z 45

3.8 Response Curves From Out-of-plane Sine Sweep, X 45

3.9 Response Curves From Out-of-plane Sine Sweep, Y 46

3.10 Response Curves From In-plane Random, Z 47

3.11 Response Curves From Out-of-plane Random, X 48

3.12 Response Curves From Out-of-plane Random, Y 48

3.13 Max Stress From In-plane Random Vibration Sweep 51

3.14 Max Stress From Out-of-plane Random Vibration Sweep 51

3.15 Max Stress From In-plane Sine Sweep 53

3.16 Max Stress From Out-of-plane Sine Sweep 53

3.17 Sensitivity Study of Element Size 55

4.1 Bounding Box for Heat Pipe Evaporator Placement 58

4.2 Potential Printing Configuration 60

NOMENCLATURE

A	Area [m^2]
α	Absorptivity [-]
ASD	Power Spectral Density [g^2/Hz]
ΔT	Finite Temperature Difference [C]
E	Young's Modulus [MPa]
$\mathcal{E}$	Emissivity [-]
f	Frequency [Hz]
g	Gravity [m/s^2]
G	Thermal Conductivity [W/K]
k	Thermal Conductance [Wm/K]
L	Length [m]
NU	Poisson's Ratio [-]
μ_v	Vapor Viscosity [Ns/m^2]
P_v	Saturation Pressure [pa]
q	Flux [W/m^2]
Q	Power [W]
r_v	Radius of Heat Pipe [m]
R	Thermal Resistance [K/W]
R_{gas}	Gas Constant
ρ_v	Vapor Density [kg/m^3]
T	Temperature [C]
σ	Stephen Boltzmann Constant [5.67×10^{-8} W/m^2K^4]
θ	Angle [degrees]

CHAPTER 1: INTRODUCTION

In order to proceed with the thermal and structural analysis of the novel 3D printed heat pipe structures, it is essential to gain an understanding of the current systems in question. The study conducted in this thesis will revolve around the 3U CubeSat form factor (30cm x 10cm x 10cm). 3U CubeSats were chosen for this analysis as they are an affordable platform for universities and private companies that are increasing in capability and popularity with 921 launches from the years 2018 – 2021 and an expected 2685 launches in the coming four years, 2022 – 2025, an almost 300% increase in launches in the coming three years [1]. These CubeSats generally use passive thermal controls and mechanical structures primarily made of 6061-T6 Aluminum. Passive thermal controls are easier to implement into these platforms as they are cost-effective, relatively simple, and adequate for most of the requirements for thermal management to date. These systems, for the most part, include thermal straps, radiators, thermal isolators, etc. However, this traditional methodology begins to have drawbacks, as new, affordable SmallSat technologies are increasing the thermal management requirements beyond the effectiveness of traditional passive thermal control systems.

Structural and thermal analyses are performed using the Phoenix CubeSat as a model, as it is a baseline representation of nominal power usage for SmallSat missions. Phoenix was a 3U CubeSat developed by Arizona State University (ASU), which used infrared imaging to study the Urban Heat Island Effect in US cities. The spacecraft had a peak power draw of 8W, and thermal control was managed using traditional passive thermal controls, including a simple radiator with traditional conductive paths to electronic components. To this nominal CubeSat, an additional component is added to

represent an advanced Graphics Processing Unit (GPU) commonly found on small spacecraft. The GPU used for this extra heat load is the NVIDIA Jetson TX2, which, when added to this configuration, effectively raises the power usage of the CubeSat from 8W to 28W~30W. With power delivery systems being designed for peak power draws of 40W [3] for these platforms, this power density now requires a novel form of thermal management. This study aims to show that 3D printed heat pipes can be incorporated into a SmallSat chassis, increasing their thermal management capabilities while retaining the structural requirements necessary to be flight worthy.

1.1 OBJECTIVES

The main objectives of this study are to:

1. Design a 3D printable heat pipe structure that can be incorporated into a 3U chassis platform that increases the thermal management capabilities of said structure.
2. Conduct thermal finite element analysis of these novel structures.
3. Conduct structural finite element analysis of these novel structures.

This study will be using commercial off-the-shelf components to create a baseline metric for thermal load and make additions that raise the thermal management requirements of the 3U platforms by using high power dense components.

1.2 3U CUBESAT OVERVIEW

The Phoenix CubeSat, developed by ASU (Figure 1.1), presents an example of a traditional 3U CubeSat.

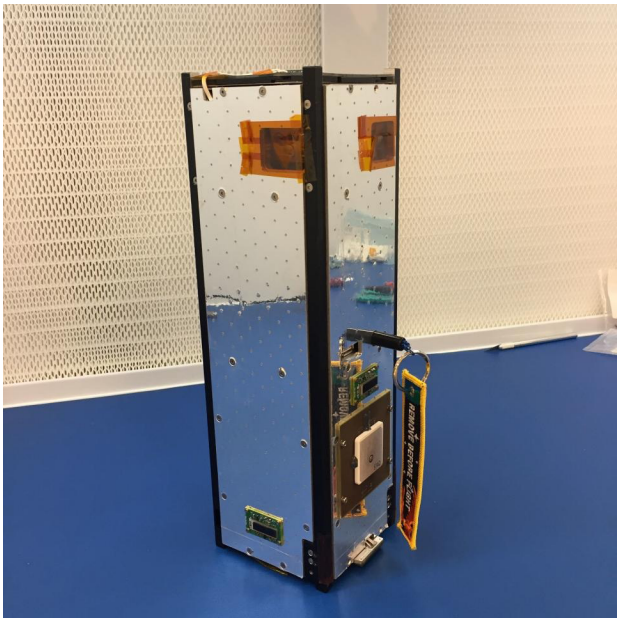

Fig 1.1 Assembled Phoenix CubeSat

Passive thermal controls were implemented for temperature management, with cooling being done by optimized thermal conductive paths to the radiator of surface area 0.03m^2. This effective conductance path from the major heat sources, electronics package, to the radiator is approximately 0.74 W/K. This will be shown later to be much lower than what is achievable with a heat pipe added to the thermal resistance network. Hot case temperatures under normal operational loads in Table 1.1.

Table 1.1. Nominal Operating Temperatures of Phoenix CubeSat

Phoenix CubeSat Electronics Temperature State – Nom. Power Density			
Component	Operating Temp (C)	Max Temp (C)	Min Temp (C)
Batteries	5 to 42	40.46	39.5
NanoMind	-30 to 85	56.9	56.2
Avg E-Stack	varies	45.7	41.7

As shown, there is little error margin in exceeding the maximum allowable operating temperatures. If the heat load is more than doubled to raise the electronic package from 4.5W to 20W, the temperatures exceed maximum allowable operating conditions, as seen in Table 1.2.

Table 1.2. Hypothetical Overpowered Temperatures of Phoenix CubeSat

Phoenix CubeSat Electronics Temperature State – Higher Power Density			
Component	Operating Temp (C)	Max Temp (C)	Min Temp (C)
Batteries	5 to 42	53.4	52.6
NanoMind	-30 to 85	64.4	62.2
Avg E-Stack	varies	61.9	52.9

This is the basis of introducing an integrated heat pipe solution for these SmallSats, which allows for proper thermal management of higher power components but does not impede on the limited volume available for internal payloads or reduce the

structural performance. For purposes of this analysis, the nominal power density of a 3U CubeSat will be defined as 4.7 x 10^3 W/m^3 and high-power density of 1.0 x 10^4 W/m^3, will be used. Based on SmallSat power draws outlined in [10], nominal power usage will be defined as 7W - 20W, and average power draw as 14W. Moving forward with the analysis of the novel heat pipe structure, 14W will be considered a nominal power draw for a 3U CubeSat and 28W will be the design goal for power management on a high-power dense CubeSat configuration.

1.3 HEAT PIPES

A heat pipe is a sealed container in which a fluid is continuously evaporating and condensing, thereby establishing a two-phase system resulting in essentially constant temperature throughout the container [7]. A classic example of a heat pipe configuration are closed loop heat pipes like the one shown in Figure 1.2.

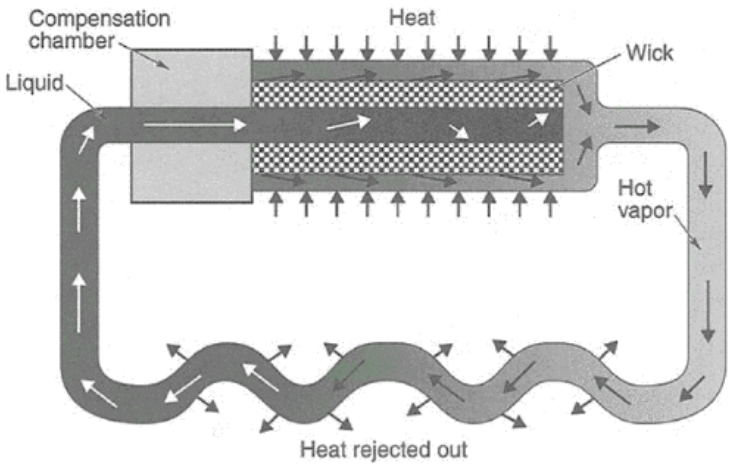

Fig 1.2. Closed Loop Heat Pipe Diagram [9]

These types of heat pipes consist of an evaporator, condenser, and transport lines. This is the kind of heat pipe chosen for this design. Looped heat pipes (LHP's) allow for a relatively more straightforward configuration and only require a wicking structure in the evaporator zone ('Heat' region, described in Figure 1.2) [8]. The wicking structure itself is the most challenging portion of the heat pipe to 3D print due to the resolution of current additive manufacturing capabilities. Adding secondary wicks is not necessary; they merely enhance performance and robustness and help adapt an LHP to zero-g applications [8].

Traditionally, heat pipes are extruded from copper tubing and crimped at the ends after they have been filled with a working fluid. However, with the advent of additive manufacturing, plenty of research has gone into the field of 3D printing heat pipes. These are generally not made from copper but other metal alloys such as Inconel, stainless steel, or AlSi10Mg using Direct Metal Laser Sintering (DMLS) printing, similar to work

mentioned in Section 1.4 by Chang et al. [4]. As a result, we can expect a performance of heat pipes ranging from 4,000 to 100,000 W/mK with a more precise range for electric cooling applications, more like 1,500 to 50,000 W/mK [12]. This is a vast improvement over copper or graphite thermal straps ranging from 450 to 3500 W/mK, respectively.

1.4 CURRENT DESIGN

The design used for this analysis consists of a closed loop heat pipe integrated into one of the structural walls of a 3U CubeSat bus. This heat pipe uses the spacecraft radiator to cool the condenser section and the heat produced by the electronics to the evaporator section. A cross-sectional view of the heat pipe integrated into the CubeSat bus is shown in Figure 1.3.

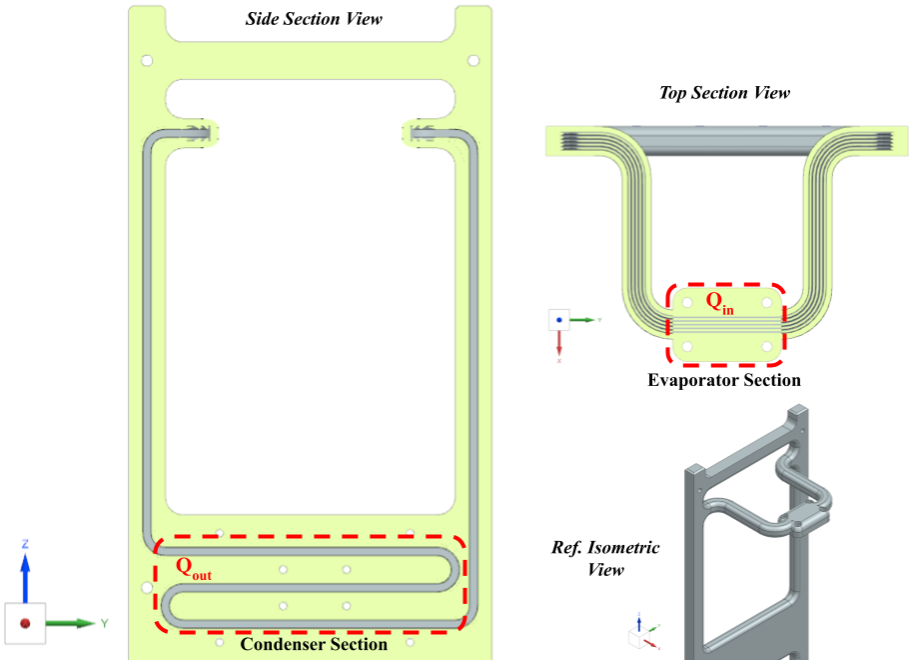

Fig 1.3. Cross-sectioned Views of Current Heat Pipe Structure

As the goal of this study is not to design the specific geometry for a heat pipe, this analysis will leverage work done by Chao Chang [4] to demonstrate the viability of 3D printing the heat pipe geometry shown in Figure 1.4 for thermal controls in small spacecraft. This geometry consists of a grooved wicking structure with grooves of approximately 1mm in height and 0.9mm in base length and produces an effective thermal conductivity of 20,803 W/mK [4] in their configuration.

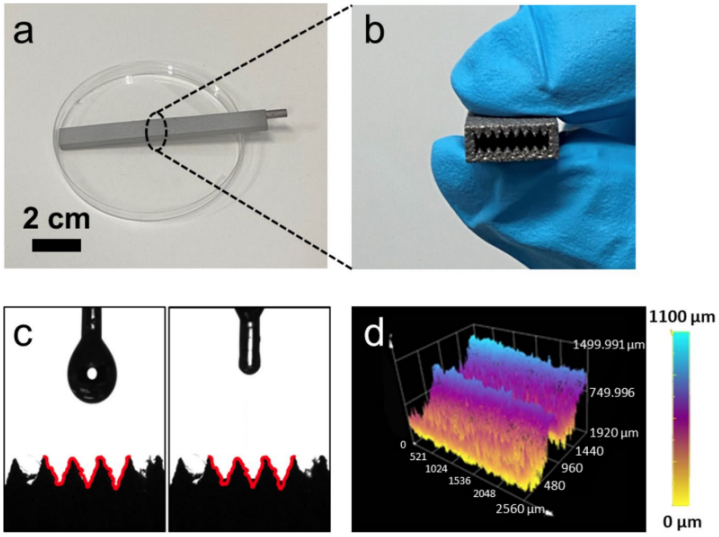

Fig 1.4. Printed and Tested Heat Pipe, Chao Chang

This grooved wicking structure geometry was chosen for this study mainly for the fact that this creates an entirely hollow section inside the structural wall of the spacecraft bus that is simpler to print as opposed to a meshed wick. While work done by Chang showed a high effective thermal conductivity using acetone as a working fluid, the hollow internal section requires further evaluation to prove it would not be damaged due to the

high loads experienced during launch. This analysis's actual heat pipe structure has an effective condenser length of 0.251m and evaporator length of 0.03m. The heat pipe length is 0.337m in total, which yields an effective length, $l_{eff,}$ of 0.299m.

$$l_{eff} = \frac{l_{condeser} + l_{evaporator}}{2} + l_{heat\ pipe} \qquad (1)$$

It is important to note that because of the nature of 3D printing this structure, the actual location of the evaporator can be moved along the Z-axis to more efficiently place it near or on top of the high heat load component regardless of its location inside the CubeSat, as shown in Figure 1.5. As a result, the effective length of the heat pipe can vary from 0.159m to 0.412m.

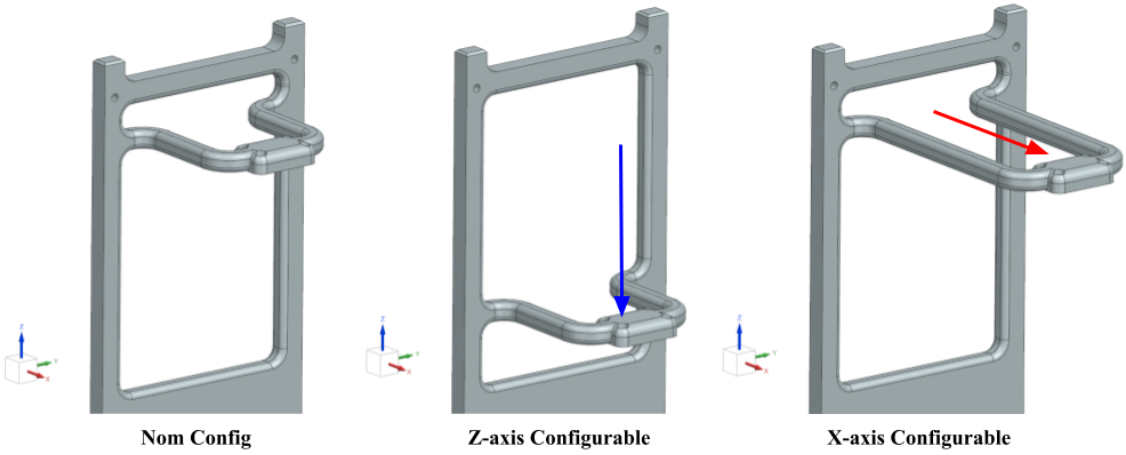

Fig 1.5. Versatility of 3D Printed Heat Pipe Structure

The heat pipe structure has a current cross-sectional area of 4.3 x 10^{-5} m^2 with a groove wicking structure with dimensions of 0.9mm base width and 1mm height, as these can be

printed within the current constraints of DMLS printing [6]. The material used for this study is AlSi10Mg which has excellent mechanical and thermal properties that are comparable to Aluminum 6061-T6, as seen in Table 1.3.

Table 1.3. Thermal Mechanical Properties of AlSi10Mg

AlSi10Mg Thermal Conductivity	
Material State	Thermal Conductivity *K*, W/mK
As Manufactured	105
Stress Relieved	165
Aluminum 6061-T6	167

With those properties defined, the heat pipe's effective conductivity (K_{eff}) is determined by Eq. 2 as 66,711.07 W/mK, using the standard effective length shown in model images and a range of 41,853.68 to 77,184.68 W/mK, with a shorted and lengthened heat pipe structure shown in Figure 1.5.

$$K_{eff} = \frac{Q*l_{eff}}{A*\Delta T} \qquad (2)$$

Both high and low values assume a conservative ΔT of 5° C between the condenser and evaporator, which will be shown later to be 2.4° C, as well as a heat input of 20W to the evaporator.

From this design we can also analytically estimate the max transport power ($Q_{transport}$) for this heat pipe design using a simple conduction model from [15]. This analysis will require the working fluid's definition for the temperatures in which this configuration is expected to operate (<50°C). Acetone was chosen as the working fluid as it has an operational working temperature range from 0°C to 120°C [14]. Acetone is also compatible with aluminum, the material used for the heat pipe structure in this study. Methylamine, pentane, and propylene also have similar working temperature ranges; however, due to the desire to maintain a design that is easy to manufacture, test, and use, acetone is the ideal choice. Therefore, the working fluid itself does not have a major effect on the performance of the heat pipe in this use case. The thermomechanical properties of Acetone at 40°C are shown in Table 1.4 [16].

Table 1.4. Thermophysical Properties of Acetone

Acetone Thermophysical Properties at 40°C	
R_{gas}	143.2
μ_v, kg/ms	8.6×10^{-6}
ρ_v, kg/m^3	1.05
P_v, N/m^2	5.0×10^4

Based on equations in [15], the max power transport limit for the heat pipe is defined as:

$$Q_{transport} = \frac{\Delta T_{evap-amb}}{\frac{t_w}{k_w A_{evap}} + \theta_{adiabatic} + \frac{t_w}{k_w A_{condensor}} + \theta_{hs}} \quad (3)$$

Where the thermal resistance of the adiabatic section of the heat pipe, $\theta_{adiabatic}$, is defined as [15]:

$$\theta_{adiabatic} = \frac{l_a}{k_{vapor} A} \quad (4)$$

And finally, the thermal conductivity of the vapor, k_{vapor}, is defined as [15]:

$$k_{vapor} = \frac{L^2 p_v \rho_v r_v^2}{8 R \mu_v T^2} \quad (5)$$

Solving these three equations, yields a max transport power limit of:

$$Q_{transport} = 19.97\ W$$

As a result, the novel heat pipe structure can manage a total of 19.97 W, leaving 8W to be managed by conventional passive thermal management techniques. This is advantageous for SmallSat platforms, as it allows the spacecraft to expand from the traditional 8W power consumption to include an additional 20W for high power components.

The condenser end of the heat pipe requires a conductive path to the spacecraft radiator, which will act as a heat sink, as shown in Figure 1.6. Initially, the condenser end of the heat pipe initially had eight 2-56 bolted connections, which yielded a total thermal conductance of 1.68 W/K. However, this was found to be too low and created a concentrated hot zone on the radiator. To remedy this, a Thermal Interface Material

(TIM) was introduced to be in-between the condenser section and radiator. Indium was chosen as the TIM, which has a thermal conductivity of up to 80 W/mK.

$$G = \frac{K*A}{L} \qquad (6)$$

Assuming a TIM layer thickness of 0.005in and 0.004m^2 for the contact area between the condenser section and the radiator, yields a total conductance to the radiator from the condenser of 2519.7 W/K, which is sufficient for this interface to not be a thermal bottleneck for the heat pipe condenser to its thermal sink. The introduction of the TIM overrides the concentrated thermal conductive path created at a bolted region and assumes the faces can make a near-perfect contact, also pictured in Figure 1.6

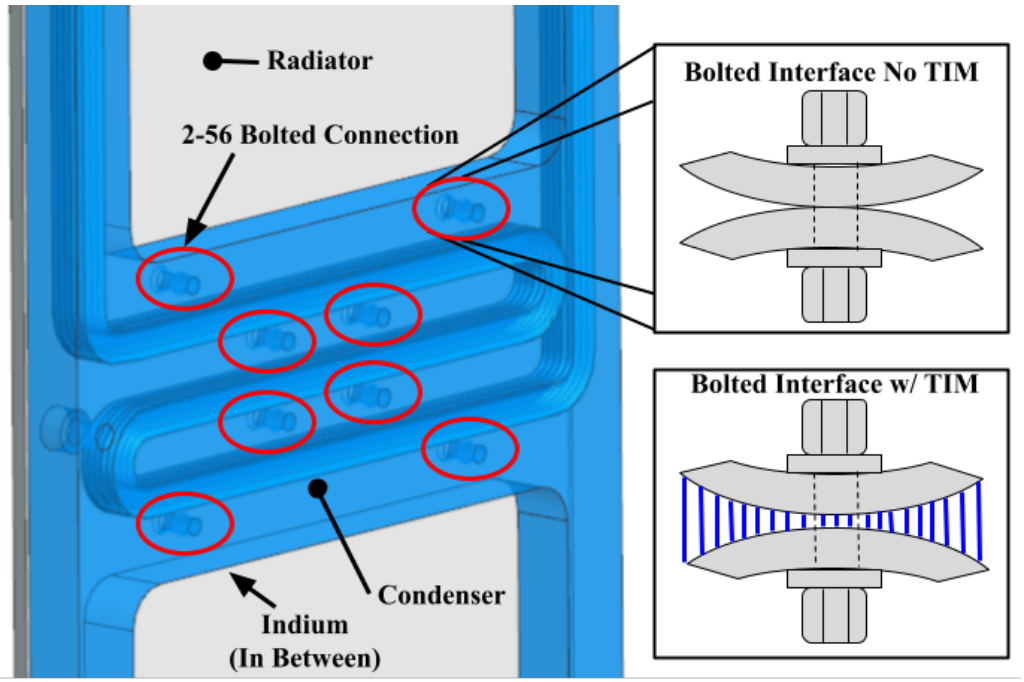

Fig 1.6. Thermal Interface Connection of Heat Pipe Condenser

In addition to the contact between the condenser and radiator, the rest of the heat pipe structure must also have a high thermal conductivity. Isolating the heat pipe from the rest of the structure was considered, but this created a localized hot spot near the center of the radiator, resulting in reduced efficiency from the large temperature gradients across the face of the radiator. As a result, the rest of the heat pipe structure also has Indium as a TIM to the radiator. This yielded a radiator surface with even more uniform temperature distribution than the results with no TIM. The thermal resistance paths to the radiator are shown in Table 1.5.

Table 1.5. Thermal Resistances of Heat Pipe Connections

Thermal Resistances	
Location	Thermal Resistance *R*, K/W
Condenser to Radiator	3.97×10^{-4}
Structure to Radiator	0.94

CHAPTER 2: THERMAL ANALYSIS

The thermal analysis was done in the NASTRAN Space Systems Thermal solver environment. The analysis will be presented in two parts. Part I will examine the thermal performance of the heat pipe structure alone and as a complete CubeSat system, assuming steady state boundary node conditions. Part II will evaluate the thermal performance of the entire CubeSat in a nominal orbital environment in both steady state and transient

thermal conditions. Steady state models were run until a ΔT of 0.001°C was achieved between iterations. The results, shown in Figure 2.1 were achieved in 15 iterations, with the mean temperature achieved by iteration two. Transient results were allowed to run for five complete orbits, using a ΔT of 0.01°C between peak-to-peak orbit temperatures. It should be noted that internal component radiation was omitted after conducting an impact trade study, which showed that internal radiation only made internal temperatures ~2°C cooler. Since exceeding allowable hot temperatures is the major concern for this study, omitting internal radiation increases thermal design margin by working with hotter temperatures and reducing the computational time per iteration. The overall goal of these simulations is to show that this heat pipe structure can manage the higher heat load by keeping the max operating temperature of high-power components below a limit of 50°C. This limit was selected based on the average operating temperature limit of the Phoenix CubeSat components.

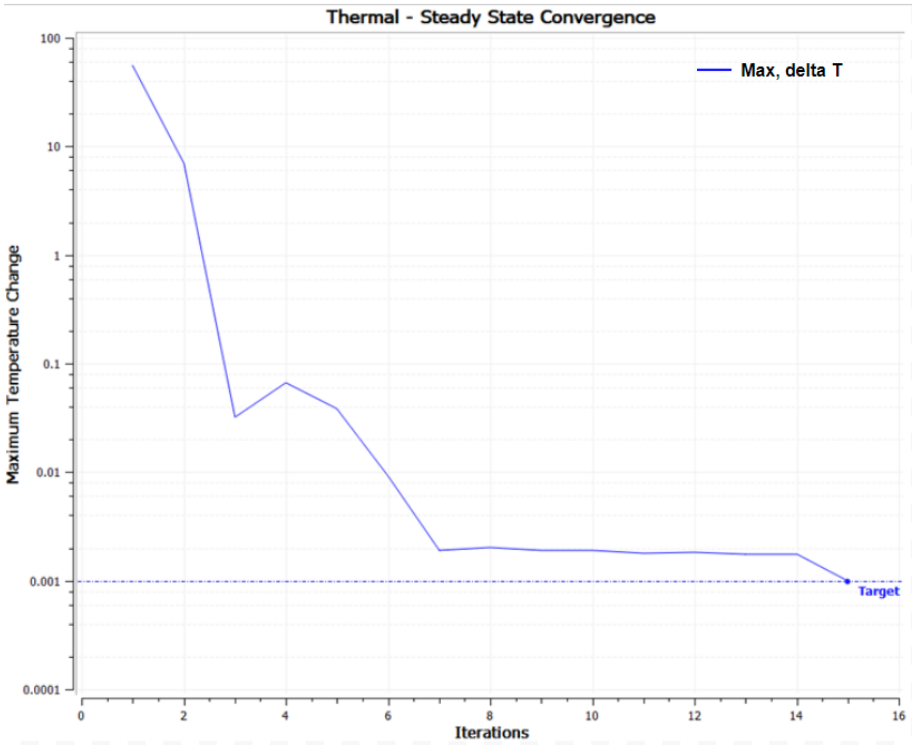

Fig 2.1. Simulation Convergence Criteria

Before looking at the simulation results, it is prudent to review steady state heat flow maps of the entire system and the heat pipe structure alone to correlate with simulation results. It is important to note here that simulation results will be validated in the form of analytical analysis and will not be verified with physical testing. Figure 2.2 below shows the entire CubeSat structure's simplified heat flow block diagram.

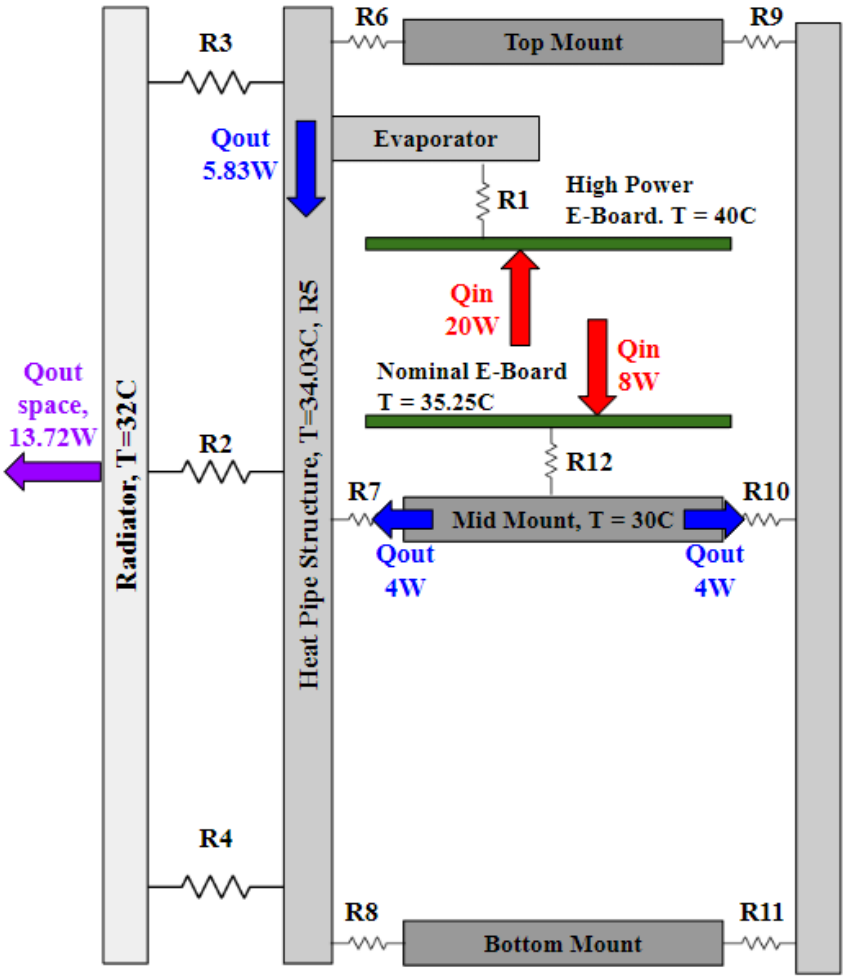

Fig 2.2. Heat Flow Map of Entire CubeSat System

Per Figure 2.2, two electronics boards are added to the system. The top board, thermally bound to the evaporator section of the heat pipe structure, will represent a power dense electronics board like a Jetson TX2 GPU or any other high-power consumption Commercial-off-the-Shelf (COTS) component. This board has a representative power consumption of 20W. The bottom electronics board represents a standard 3U CubeSat electronics stack with a nominal power consumption of 8W. This

produces a total internal power load of 28W, excluding heat loads caused by the orbiting environment. Although not represented in the image, the outer panels of the CubeSat are subjected to a total of 14.5W from solar and Earth albedo/IR heat fluxes.

The heat flow map, shown in Figure 2.2, provides a basis for mapping the thermal resistance networks for the power dense electronics board and the nominal electronics board. The resistance network below represents the thermal resistance path from the power dense board (through the evaporator) to the spacecraft's radiator.

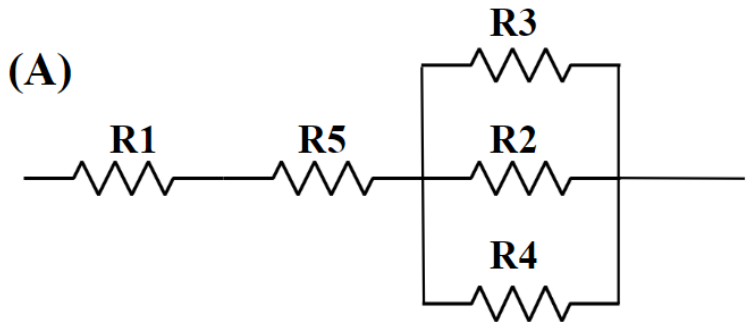

Fig 2.3. Thermal Resistance Network from Evaporator to Radiator

Here, R1 represents the thermal interface to the power dense electronics board's evaporator section. Applying a highly thermally conductive TIM to this interface, the conductance is calculated using Eq. 6 as 220.62 W/K. R2 represents the thermal interface from the condenser section to the radiator. Using a highly thermally conductive TIM for this interface as well, the thermal conductance was calculated as 2519.7 W/K. R3 and R4 are thermal interfaces from the radiator to the rest of the heat pipe structure, which produce a combined total of 0.94 W/K. Finally, R5 is the effective thermal

conductivity of the heat pipe, which is found from the effective thermal conductance found earlier (66,711 W/mK) multiplied by the effective heat pipe length (0.337m). This yields a conductance of 22,481 W/K. Solving for this resistance path yields an effective thermal conductivity of:

$$G_{A,reff} = 9.59\ W/K$$

Although this is the pure resistance path to the radiator from the evaporator, there is some efficiency loss to the rest of the structure in the form of resistances R6, R7, and R8. These represent bolted connections between the heat pipe and the rest of the satellite, resulting in a total conductance of 1.06 W/K. Using the thermal resistance values found above and assuming the temperature of the power dense board reaches 40°C (placing a 10°C margin on the maximum operating temperature) and a structure temperature of 41.4°C, the radiator reaches a steady state temperature of 32.2°C. 13.38W is radiated into space and 5.83W is lost to the rest of the CubeSat structure. Per the analysis described in Section 2.4, this analytical calculation is ~ 5°C away from steady state simulation results. It should be noted that this assumes a uniform radiator temperature, which in practice is difficult to achieve and will be discussed more later in this section. These analytical calculations also show a 5°C temperature difference from the evaporator to the condenser section. The radiator is assumed to have the properties shown in Table 2.1 and assumes a full view factor to space.

Table 2.1. Tabulated Spacecraft Radiator Properties

Spacecraft Radiator Properties	
Area, m^2	0.0302
Emissivity, Ɛ	0.9
Temp, C	34.4

It is important to expand a bit more on the spacecraft radiator. As mentioned, the steady state hand calculations assume a uniform temperature distribution across the surface of the radiator, which itself is a 2mm thick sheet of aluminum. However, after running steady state simulations for the system in NASTRAN (see Section 2.5), there is a 14°C temperature gradient across the radiator surface with a temperature range of 30.52°C to 16.41°C, producing an average radiator face temperature of 27.04°C, as shown in Figure 2.4. This temperature gradient can be partially attributed to the fact that even though there is a large thermal conductance to the radiator from the condenser section of the heat pipe, the thermal conductance through the radiator is very low as it has a small cross-sectional area. With this, the total effectiveness of the radiator as a heat exchanger can be evaluated using Eq. 7.

$$\varepsilon = \frac{Q}{Q_{max}} \qquad (7)$$

Q_{max} was found by assuming the radiator has a uniform temperature of 30.52°C and yields a radiating power of 14.45W. Q was found by using the actual average temperature across the radiator face of 27.04°C and yields a radiating power of 13.8W. With these two

values the total effectiveness of the radiator was found to be 0.95. For the purpose of this study the 4.5% loss in radiator performance will be accepted as a detailed radiator design can be its own research topic. Given the temperature gradient across the radiator and its small thickness, the potential of a large deformation should be quickly addressed.

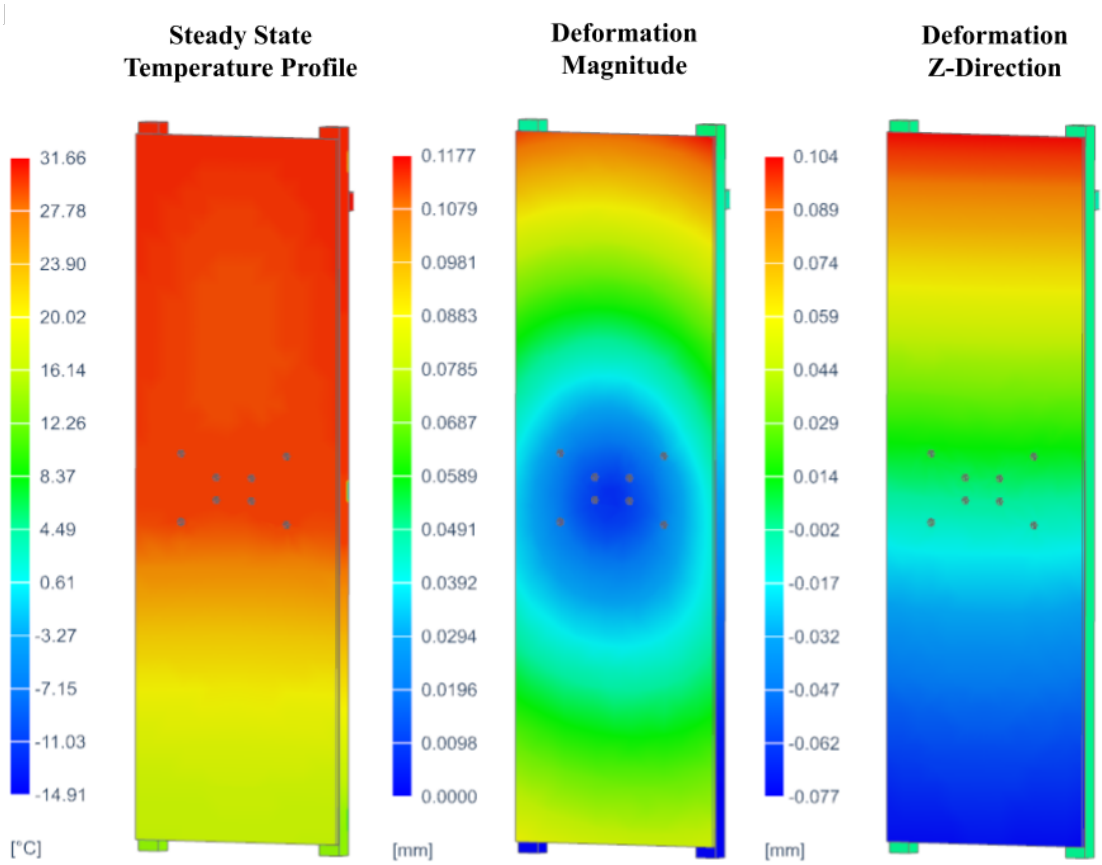

Fig 2.4. Radiator Temperature vs. Displacement Comparison

Per Figure 2.4, the maximum deformation on the spacecraft's radiator, with a ΔT across the radiator of 14.11°C, is only 0.1177mm (0.0046"). This is the magnitudinal displacement across all three-cardinal axis and the largest single axis displacement in the

Z-axis being 0.104mm (0.004”). The small displacement can be partially attributed that there does not exist a large difference in the coefficient of thermal expansion (CTE) between the radiator and the heat pipe structure it is attached to as the CTE of Aluminum 6061-T6 and AlSi10Mg are nearly identical. Therefore, given this small displacement on the thin radiator and the temperature gradient across it, we will not be treating this as a source of mechanical design concern.

Going back to the thermal resistance paths for the electronics boards, we can do a similar analysis for the heat flow of the bottom nominal electronics board, following the thermal resistance path B shown in Figure 2.5.

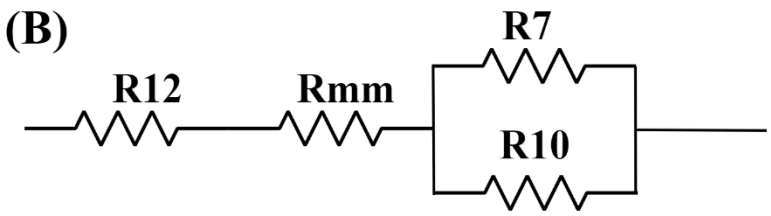

Fig 2.5. Thermal Resistance Network from Nominal Board to Structure

In this thermal resistance map R12 represents the thermal interface between the bottom electronics board and some mount near the center of the spacecraft, five 10-32 screws, with a total conductance of 6.67 W/K. R_{mm} represents the thermal resistance of said mount, totaling 50 W/K. R7 and R8 are bolted connections from said mount to the rest of the spacecraft structure, totaling 1.04 W/K each. Solving for this resistance path yields an effective thermal conductance of:

$$G_{B,reff} = 1.51\ W/K$$

With these values and assuming the temperature of the bottom electronics board reaches 35° C. The structure will reach a temperature of 30° C from an 8W power input from the bottom electronics board.

Similarly, we can look at the external loads and management by the spacecraft structure and remaining structure panels. A few assumptions will be made here about the panels exposed to solar flux will have high emissivity and absorptivity ($\varepsilon = \alpha = 0.8$). Seen later in Figure 2.8, one panel will have a full view factor to solar flux while in the non-shaded region of the orbit, with two panels being exposed in total during the complete rotation about the orbit point. For this steady state analysis, we will assume that one panel will always have a full view factor to solar flux regardless of orbit position. With these assumptions the total thermal load induced by solar, and Earth albedo/IR will be 14.5W. This load can be managed by keeping panel temperatures at 15°C and 17°C. Given this analytical steady state analysis, we can conclude that a total of 28W of internal thermal load generation can be managed by a 3U platform with a heat pipe structure. The following section will go over the simulation results.

2.1 FEM SETUP – Heat Pipe Structure

The heat pipe structure FEM is set up in the following manner. The geometry is meshed using TET4 tetrahedral elements (4 nodes per element) with a 6mm element size and the vapor space within the heat pipe is also meshed using TET4 elements of the same size. One of the common misnomers is that heat pipes have very high effective thermal conductivity but is to be remembered that only the portion in which the vapor travels has high thermal conductivity [10]. As such the Internal vapor space has the imposed high thermal conductivity found previously of 66,711.07 W/mK and the rest of the heat pipe structure has the lower conductivity of 165 W/mK relating to AlSi10Mg. A perfect thermal contactor thermally binds together the vapor space and the heat pipe structure in the NASTRAN solver. Doing so provides a more realistic approach than imposing high thermal conductivity on the entire heat pipe structure itself. Figure 2.6 shows the two separate meshed used to define the heat pipe's solid and vapor space portion separately.

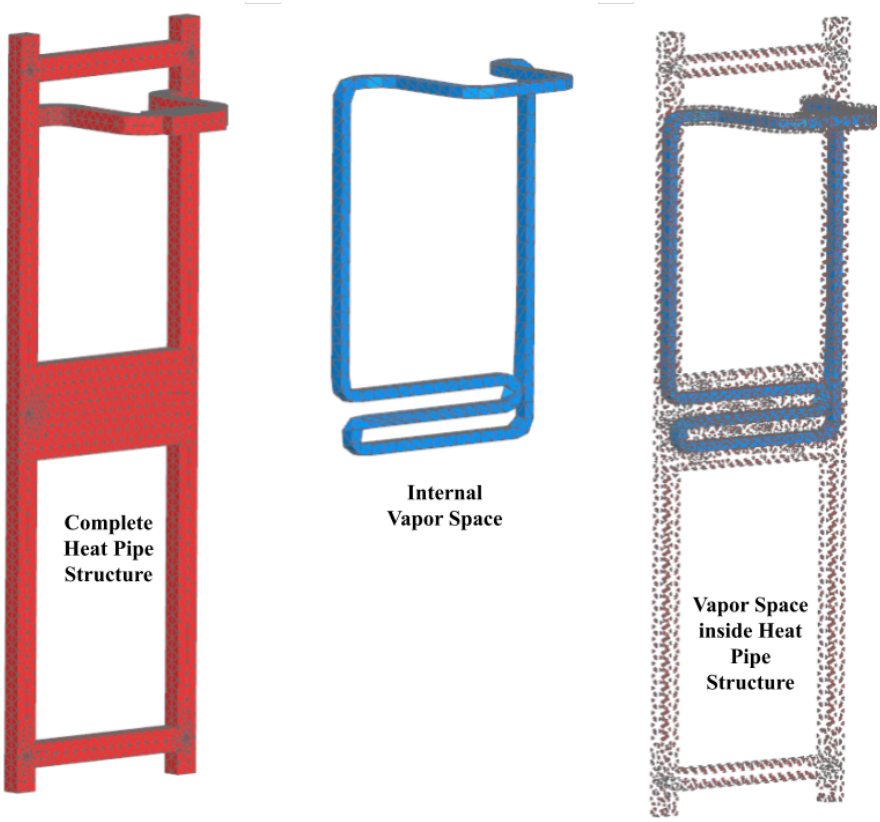

Fig 2.6. Heat Pipe Structure FEM

2.2 SIMULATION RESULTS – Standalone Heat Pipe Structure

A steady state simulation of the heat pipe structure alone was run to compare to the assumption made when solving for the effective thermal conductivity of the vapor space. From the previous section, Qmax was found to be 19.3W with a 5°C temperature difference between the evaporator and condenser sections of the heat pipe. The next figure shows the simulation setup for this analysis.

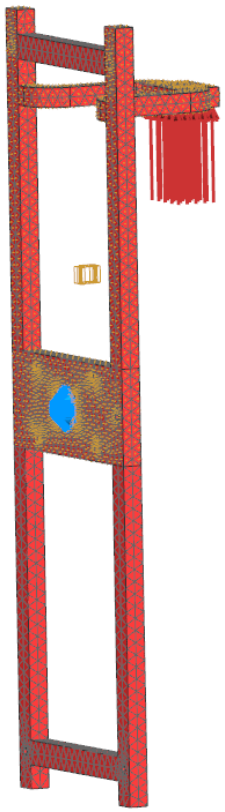

Fig 2.7. Standalone Heat Pipe Structure – SIM Setup

In Figure 2.7, the red arrows represent a 20W heat load on the evaporator section of the heat pipe structure. The blue coned region is a temperature constraint of 32° C on the condenser section of the heat pipe structure, which represents the thermal sink and was replaced by the spacecraft radiator in later simulations. In this analysis, the vapor space region (not visible) is the region with high thermal conductivity, see Figure 2.5. This simulation setup was run to steady state using the convergence criteria in Figure 2.1. The results from this simulation can be seen in Figure 2.8.

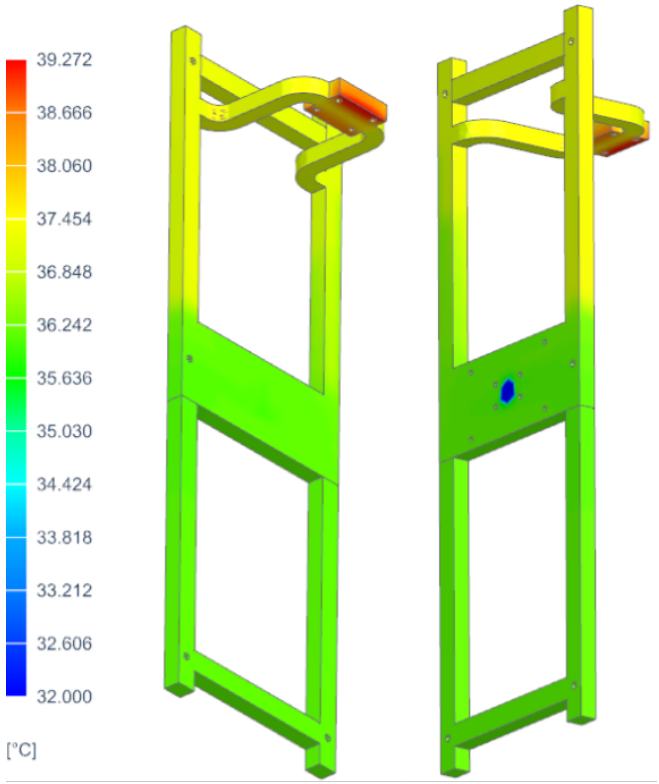

Fig 2.8. Standalone Heat Pipe Structure – SIM Results

Table 2.2. Heat Pipe Structure Alone, Tabulated SIM Results

Analytical vs Computational Temperature Comparison				
Component	Evaporator (Average)	Condenser (sink)	ΔT	%diff
Analytical Temp, C	37	32	5	-
Computational Temp, C	37.54	32	5.54	10.8

As seen in Table 2.2, the analytical and computational results agree with each other. The ΔT between the condenser and evaporator sections is 5.54°C compared to the predicted ΔT of 5°C from the hand models. This difference of 0.54°C or 10.8% error is acceptable, and we can conclude that the approach taken to model the vapor space within the heat pipe structure is valid.

2.3 NOMINAL ORBIT ENVIRONMENT

The nominal orbit environment used for the transient analysis for the analogous 3U CubeSat with the novel heat pipe structure will be a standard International Space Station (ISS) orbit at 400km with an inclination of 51.6°. This orbit was chosen as 19.6% of CubeSat launches were delivered to this orbit as of 1998, 333 of 1696 successful launches [1]. This is a standard delivery location as regular ISS resupply missions make CubeSat ride-along opportunities affordable. With that, a detailed thermal environment is seen in Table 2.3.

Table 2.3. Simulation Orbit Parameters

Thermal Environment – ISS Orbit	
Altitude, km	400
Inclination, deg	51.6
Beta Angle, deg	75.1, -75.1
Solar Flux, W/m^2	1367
Albedo and IR, W/m^2 – Hot	257
Albedo and IR, W/m^2 – Cold	218

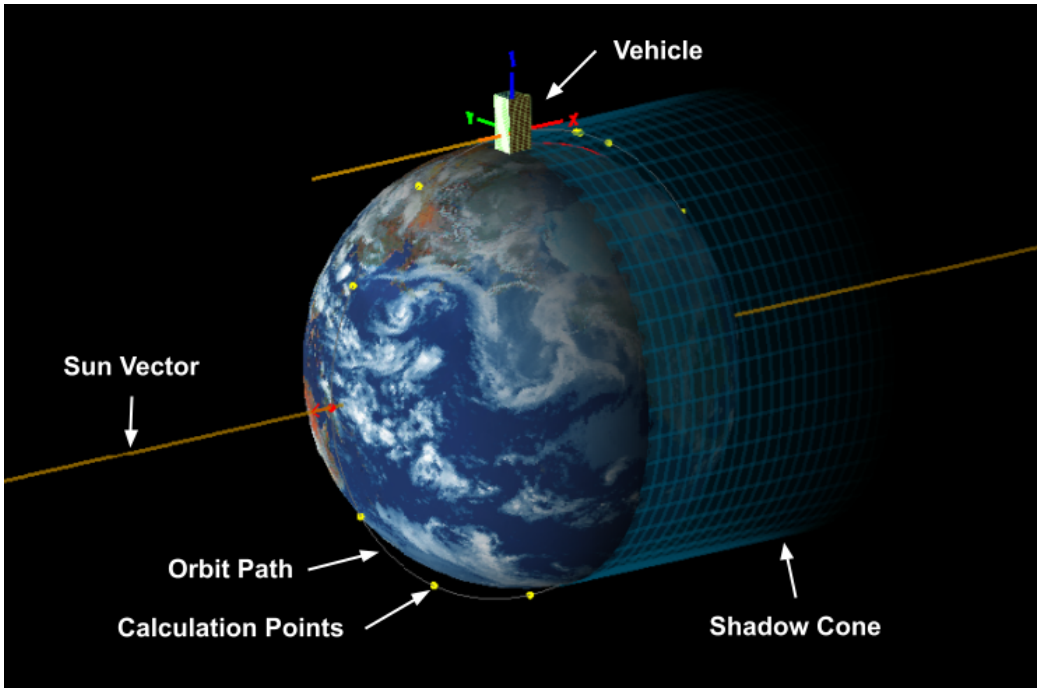

Fig 2.9. Simulation Orbit Visualization

Transient simulations will not require the addition of the solar loads shown in Figure 2.10, as the Earth's solar and albedo loads will be found at the calculation points shown in Figure 2.9 based on the vehicle's orientation with respect to the sun vector and shadow cone by the solver. It is important to note that the orientation of the vehicle was not optimized, and no vehicle rotations were considered with respect to thermal management efficiency. This was omitted to keep the orbit environment conditions as general as possible.

2.4 FEM SETUP – Entire CubeSat System

In order to analyze the use-case for the heat pipe structure in a flight configuration, a complete 3U CubeSat structure was built around the heat pipe structure along with internal electronic board heat loads. As seen in the heat flow map Figure 2.2, two electronic boards were added: one nominal power usage board and one high power board. The rest of the SmallSat structure is thermally tied together using basic common passive contactors like 4-40 screws. Figure 2.10 shows the FEM for the entire CubeSat structure.

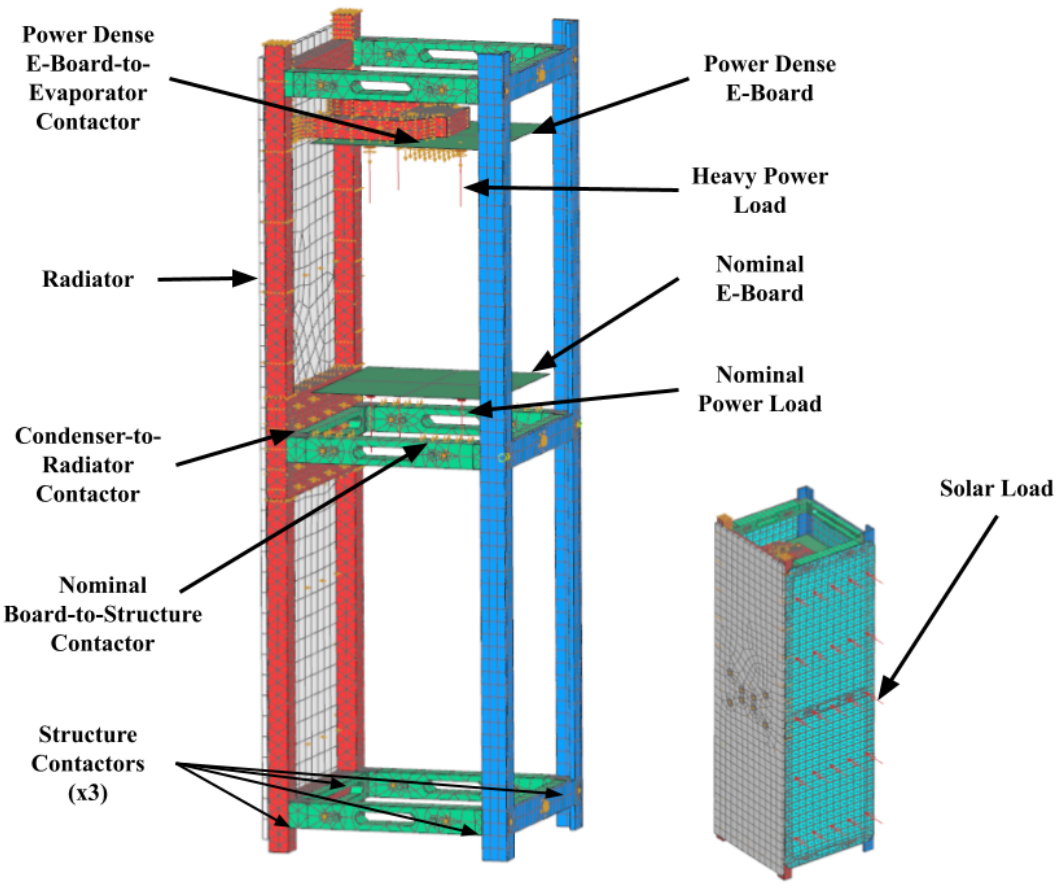

Fig 2.10. Entire Structure FEM

2.5 SIMULATION RESULTS – Entire CubeSat System, Steady State

Steady state results for the entire CubeSat system show that the temperatures of internal electronic boards do not exceed 50°C. The highest temperature seen is 41.5°C on the power dense e-board, which is directly tied to the evaporator section of the heat pipe. Tabulated steady state results below in Table 2.4, which includes the average temperature across the elements of important locations. It is important to note that these results do not use a pre-configured orbit but instead imposed solar and Earth albedo with approximate view factors on appropriate CubeSat faces. In this scenario, the temperature difference between the evaporator and condenser sections is maintained at 4.48°C.

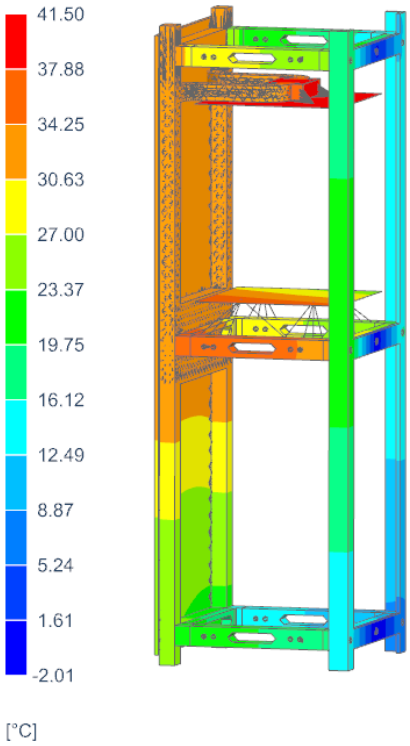

Fig 2.11. Entire Structure FEM

Table 2.4. Entire Structure Steady State Results

Entire Structure Steady State Results			
Component	Temperature, C (SIM results)	Temperature, C (Heat Flow Map)	%diff
Radiator	33.12	36.4	9.01
Power Dense E-Board	40.74	40	1.85
Nominal E-Board	38.37	35.25	8.85
Evaporator Section	38.67	37	4.5
Condenser Section	34.19	32	6.84

2.6 SIMULATION RESULTS – Entire CubeSat System, Transient

Like the steady state results for the entire CubeSat system, the transient results show that the temperatures of internal electronic boards do not exceed 50°C. The highest temperature from the simulation is 39.6° C on the power dense e-board. Seen in Table 2.4, the max temperatures on components of interest do not exceed those seen in the steady state results in the prior section. This can be because this orbit configuration does not allow enough time for the components to reach steady state while in the hot path of the orbit. The transient results offer a more accurate representation of the solar loads and space radiative cooling as opposed to the steady state results. In this scenario, the

temperature difference between the evaporator and condenser sections is maintained to 4.28° C.

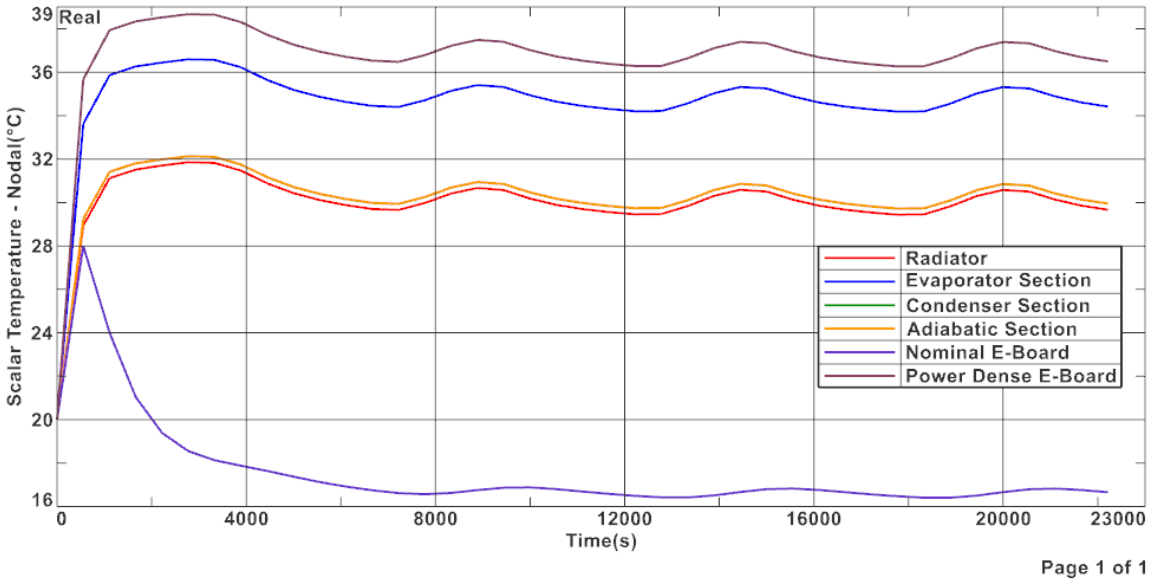

Fig 2.12. Entire Structure Transient Temperatures

Table 2.5. Entire Structure Transient Results

Entire Structure Steady State Results		
Component	Temperature, C (Min)	Temperature, C (Max)
Radiator	29.45	30.58
Power Dense E-Board	36.27	37.4
Nominal E-Board	16.49	18.67
Evaporator Section	34.19	35.13
Condenser Section	29.73	30.85

CHAPTER 3: STRUCTURAL ANALYSIS

The structural analysis for this study was constructed in the Siemens NASTRAN environment using the SOL103 Response Dynamics solver. The goal is to show that the novel heat pipe structure will not fail, exceed the yield strength of AlSi10Mg, under the largest loads this structure will experience. These being the loads experienced during launch. The Nanoracks CubeSat Deployer (NRSCD) and Interface Definition Document (IDD) will be used to define the vibration environment the structure will experience at launch. The analysis itself will use three-sigma loads for margin. Vibration environments will be defined per NRSCD:

Table 3.1. In-plane Vibration Environment

In-plane Sine Vibration Test Levels and Duration	
Frequency (Hz)	Levels (g's)
5	0.63875
24	13.8
25	13.8
26	10.8
35	10.8
40	2.4
100	2.4

In-plane Random Vibration Test Levels and Duration	
Frequency (Hz)	ASD (g2/Hz)
20	0.016
30	0.025
800	0.025
2000	0.016
grms	6.55 g's

Table 3.2. Out-of-plane Vibration Environment

Out-of-plane Sine Vibration Test Levels and Duration	
Frequency (Hz)	Levels (g's)
5	0.63875
24	13.8
25	13.8
26	10.8
35	10.8
36	6.6
50	6.6
55	2.4
100	2.4
Out-of-plane Random Vibration Test Levels and Duration	
Frequency (Hz)	ASD (g2/Hz)
20	0.016
50	0.025
800	0.025
2000	0.016
grms	8.45 g's

The in-plane direction will be defined as the Z-axis, and out-of-plane directions will be defined as the X and Y-axis. The mechanical properties of AlSi10Mg are also similar to Aluminum 6061-T6, much like its thermal properties, shown in Table 3.3.

Table 3.3. Mechanical Properties of AlSi10Mg

Mechanical Property Comparison		
	Aluminum 6061-T6	AlSi10Mg
Density	2.71 g/cm^3	2.67 g/cm^3
Youngs Modulus (E)	68,980 MPa	67,000 MPa
Poisson's Ratio (NU)	0.33	0.35
Yield Strength	241.4 MPa	230 MPa

In order to reduce the arbitrary increase of stiffness on the novel heat pipe structure by applying fixed boundary conditions on the structure that would come with running simulations on the heat pipe structure alone, a CubeSat structure was constructed around the heat pipe structure using standard designs for CubeSat busses, seen in Figure 3.1. This entire system will be used to propagate the Sine and Random Vibration curves to the whole chassis.

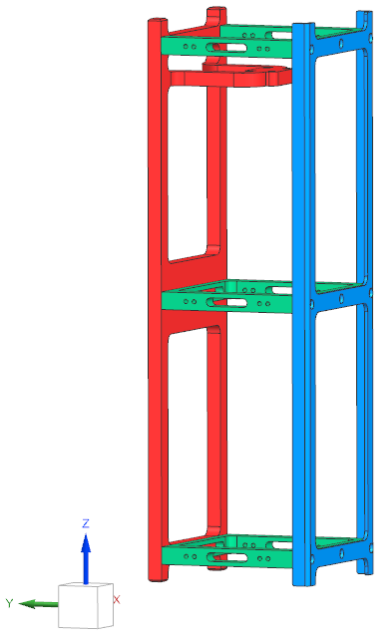

Fig 3.1. Entire CubeSat Structure

In order to create an entire CubeSat system, additional parts were constructed and are all shown in Figure 3.1. These include a -Y wall (blue) and three rib structures (green). The heat pipe structure seen in red. The structure will be fastened using 4-40 screws, six on each Y wall to the three rib structures. The total mass of this structure is 573.4g, with the heat pipe structure being 257g.

According to the NRSCD, the maximum mass for a 3U CubeSat is 4.8 kg; because of this, a 4.2 kg lumped mass will be placed in the center of mass of the CubeSat chassis to account for the realistic modes of a completed system.

3.1 FEM SETUP

The finite element modal was mainly constructed using cubic CHEXA(8) element type using ~4.5mm sized elements. Tetrahedral elements where only used in limited amounts in areas where the geometry did not allow for a clean sweep of cubic elements. The main area tetrahedral elements are present is in the heat pipe section, given there are no matching faces to push a cubic mesh through. A concentrated mass element was placed in the structure's center of gravity and is connected to the ribs using RBE3 elements so as not to impose artificial stiffness with RBE2 elements. An Enforced Motion node was placed in the -Z direction outside of the structure and will serve as the location for enforcing the sine and random vibration curves expected at launch. This node is connected to the bottom of the Y+ and Y- wall structures using RBE2 elements and is enforced in all six degrees of freedom (dofs). Bolted connections consist of CBAR elements for the bolt's shank and are connected to the surrounding structure using RBE2 elements. Bolted connection cross-section and complete structure FEM seen in Figure 3.3.

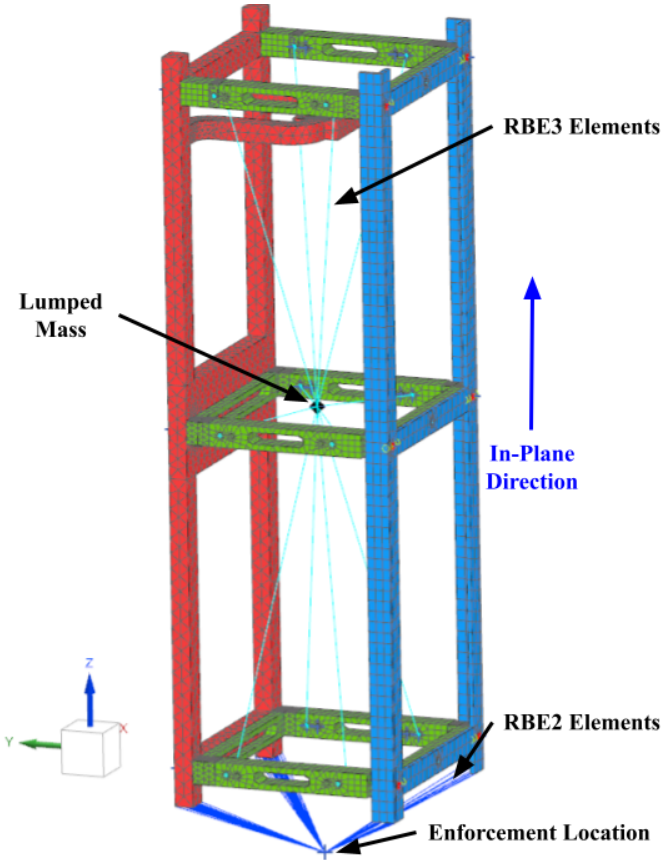

Fig 3.2. Entire CubeSat Structure FEM

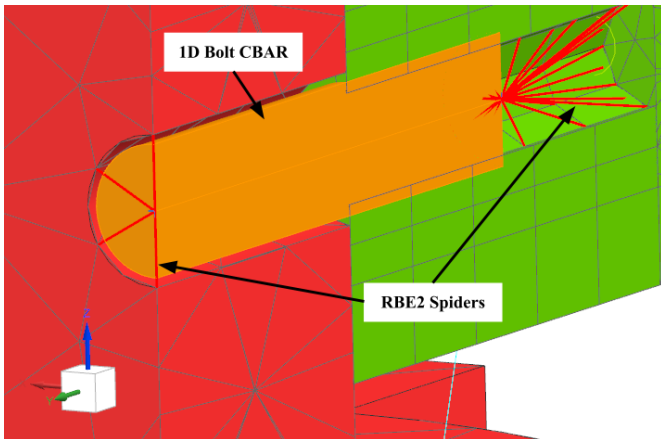

Fig 3.3. Visualization of 1D Bolted Region

The orange section in Figure 3.3 represents the 4-40 screws with an appropriate nominal diameter and has the mechanical properties of 310 stainless steel. The RBE2 spiders, in red, connect the effective threaded region to the rest of the structure. No elements in the FEM are joined together using gluing conditions; everything is mated together using appropriate bolted connections and mesh mating conditions for meshes representing the same component at the piece part FEM level. This further reduces the propagation of a stiffer than the actual structure. Figure 3.2 shows the FEM for the entire CubeSat structure along with the defined in-plane vector. A complete breakdown of the elements and total free degrees of freedom, dof, can be seen in table 3.4.

Table 3.4. Total FEM Element Breakdown

Assembly FEM Element Model Summary				
Element Type	No. Elements	No. Nodes	Free dofs	Total Free dofs
CBAR	11	2	6	132
CHEXA	4,561	8	6	218,928
CONM2	1	1	6	6
CPENTA	267	6	6	9,612
CTETRA	17,355	4	6	416,520
0D-Manual	1	1	0	0
			Total	645,198

3.2 SIMULATION RESULTS

With this FEM setup the resulting major modes of the structure in the X, Y, and Z directions are listed in Table 3.5. These modal results and the following response solutions were found using SOL 103 Response Dynamics in NASTRAN. SOL 103 performs an eigenvalue modal analysis and allows for the use of the response dynamics toolbox without having to use a separate solver.

Table 3.5. Major Modes of Structure

Major Modes			
Frequency (Hz)	X %mass participation	Y %mass participation	Z %mass participation
29.4	0	91.51	0
70.7	91.45	0	0
408.1	0	0	90.85

Figure 3.4 shows the expected deformation of the three primary modes. It is important to note that the deformation distances displayed in mm are arbitrary and carry no bearing as no actual force is applied when solving for the natural modes. Instead, these should be taken as overall magnitudes of deformation.

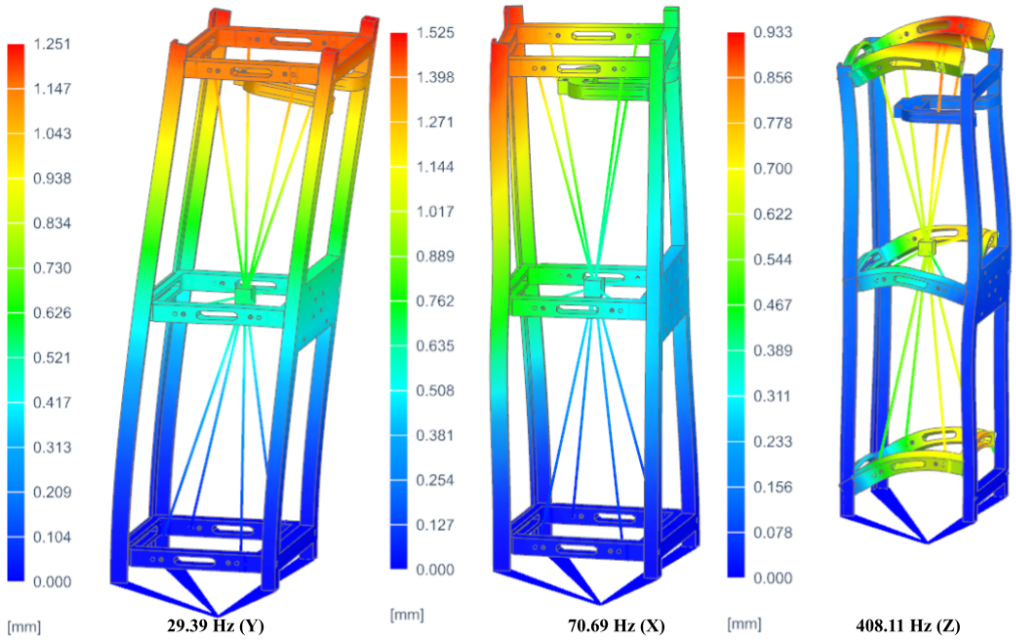

Fig 3.4. Deformation Results for Primary Modes

Although these three mode shapes correspond to the major modes of the structure, another mode of interest is at 632.96 Hz. As from the results, this mode creates a large overall deformation on the heat pipe evaporator and is shown in Figure 3.5. In reality, the evaporator section would be tied down with other components like an electronics board, but in this case, it can serve as a worst-case scenario load point.

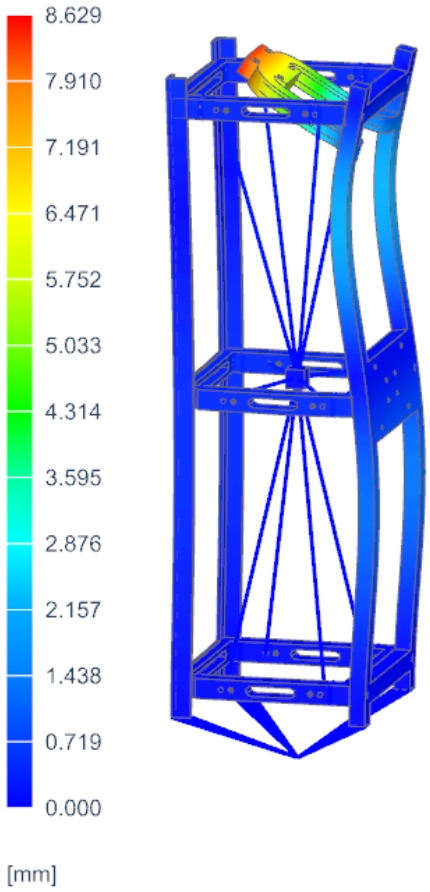

Fig 3.5. Major Mode on Heat Pipe, 632.96 Hz

From the three major modes, the X and Y modes will produce a response in the out-of-plane sine sweep for the entire structure as they are modes under 100 Hz. The in-plane sine sweep will not have a major response in the Z direction as no major Z modes are under 100 Hz. All primary modes will respond in the in-plane and out-of-plane random vibration spectral sweeps.

Propagating the in-plane sine sweep in the Z direction and out-of-plane sine sweep in the X & Y directions yielded the following response curves. Note these response curves are focused on the heat pipe structure by placing accelerometer sensors on the evaporator, condenser, and adiabatic sections. Location of the accelerometers can be seen in Figure 3.6.

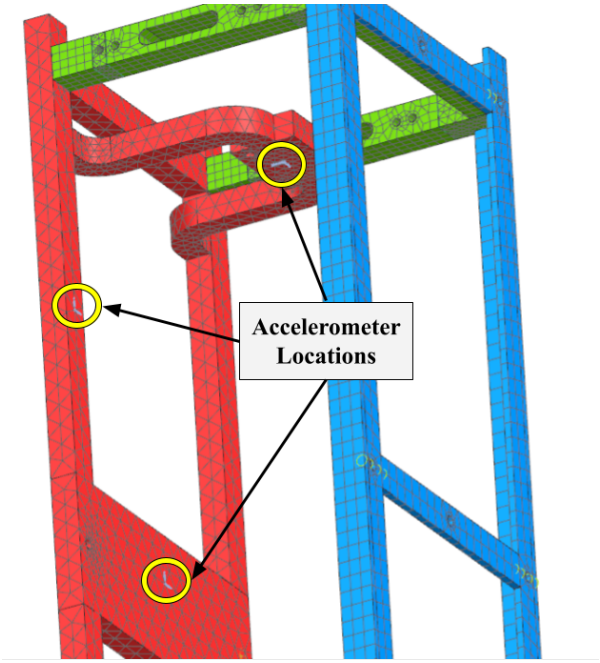

Fig 3.6. Location of Accelerometers

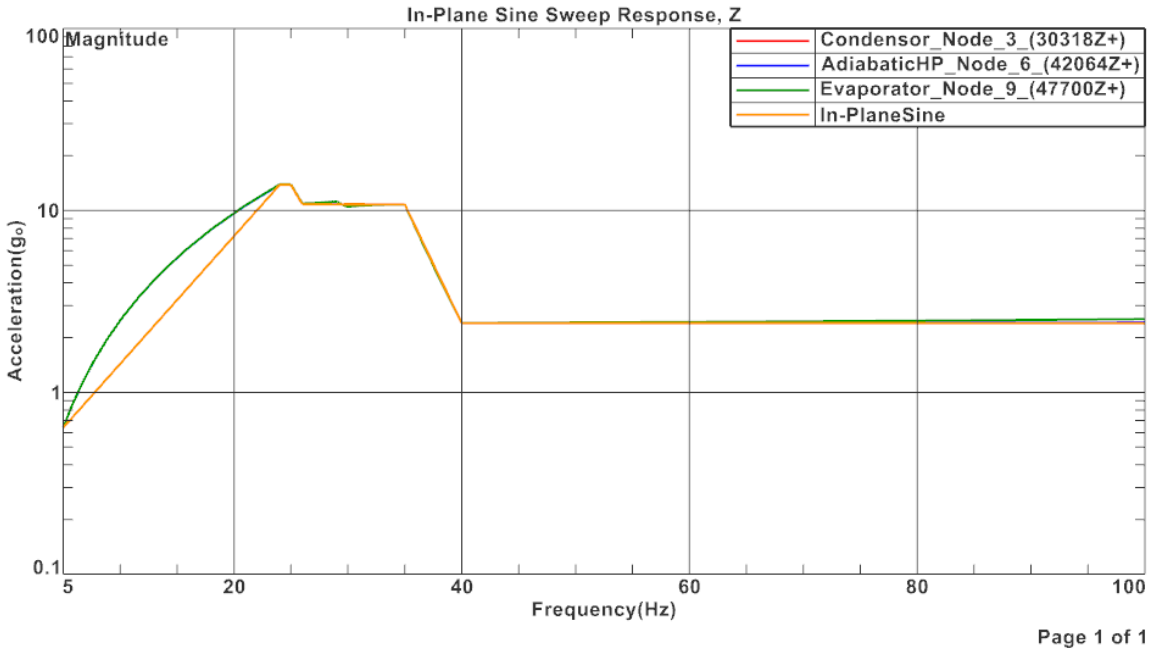

Fig 3.7. Response Curves from In-plane Sine Sweep, Z

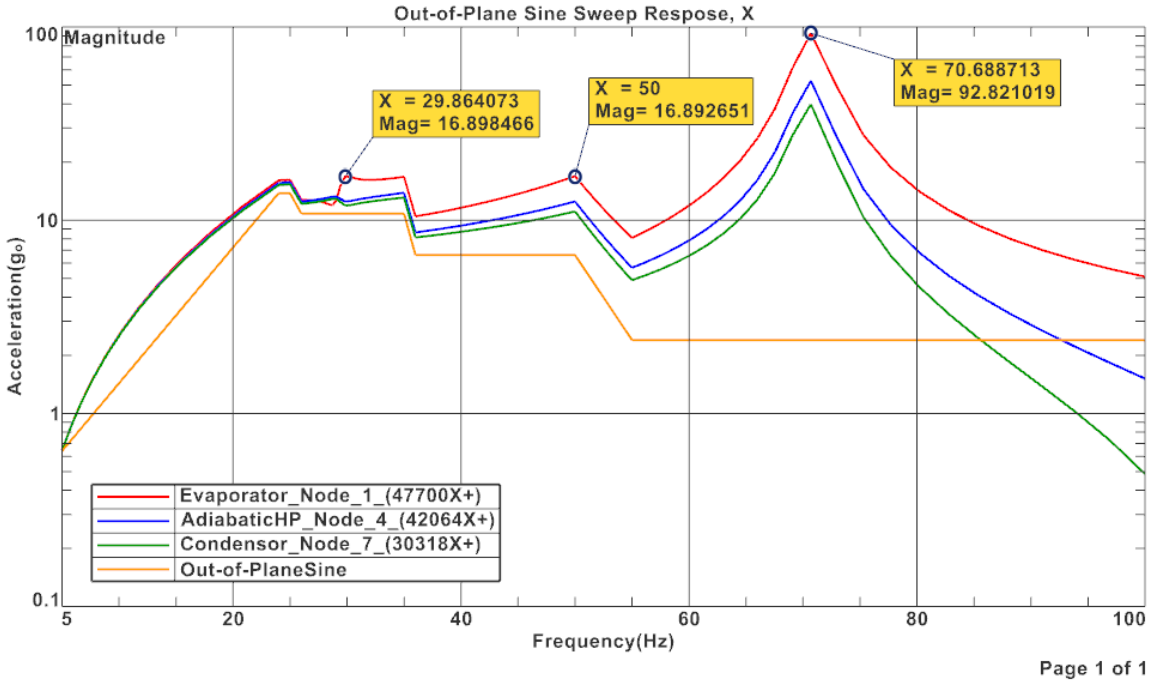

Fig 3.8. Response Curves from Out-of-plane Sine Sweep, X

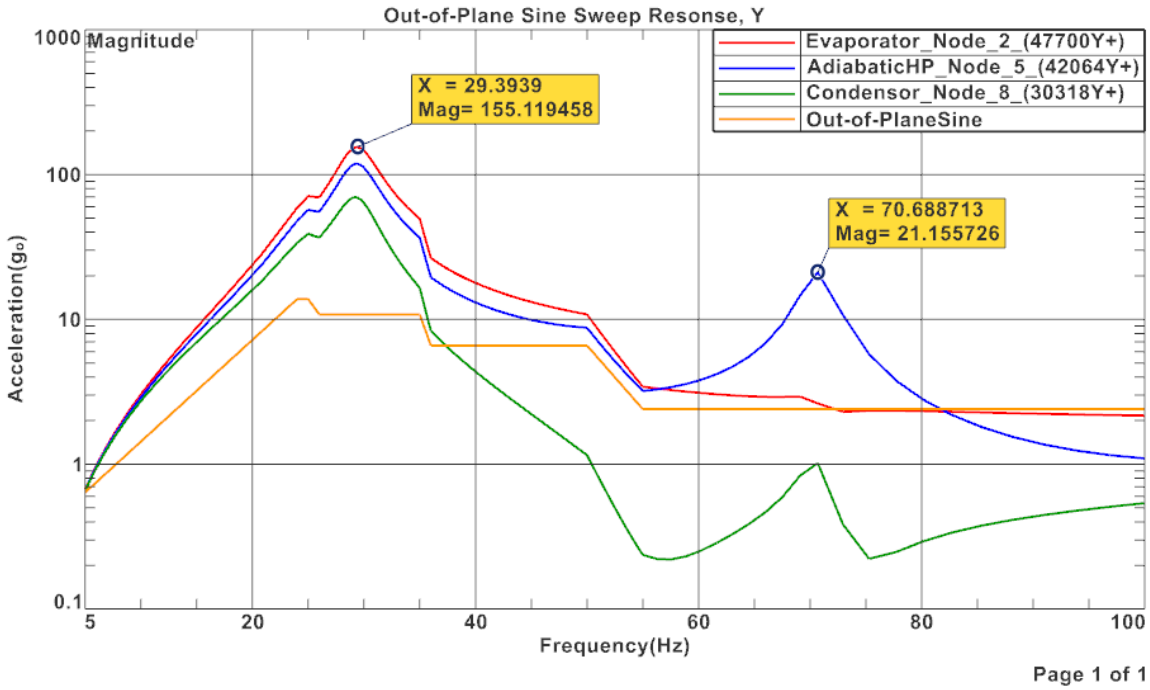

Fig 3.9. Response Curves from Out-of-plane Sine Sweep, Y

Figures 3.7-3.9 above show the responses at the accelerometers and the base sine sweep that was pushed through the structure, which is shown in orange. As expected, the in-plane sine sweep shows no response in the Z direction. However, the Y-direction response does show a spike at the expected 29.39 Hz. This response has a magnitude of 155.12 g's on the evaporator section of the heat pipe. The X-direction has a response at the expected 70.68 Hz, with a magnitude of 92.82 g's. These are high accelerations. Even though they only last for fractions of a second, they will be the source of the highest root mean square (RMS) stress concentrations, which we will look at in section 3.3. Important to note that this response and the following random vibe response have had a 2% viscous dampening factor imposed on all three major modes as this is a bolted structure and leaving the modes undamped resulted in unrealistic spikes in the response curve at all

modes in all axes. The following plots show the response curves for the In-plane and Out-of-plane random vibration sweeps in PSD, power spectral density, g^2/Hz.

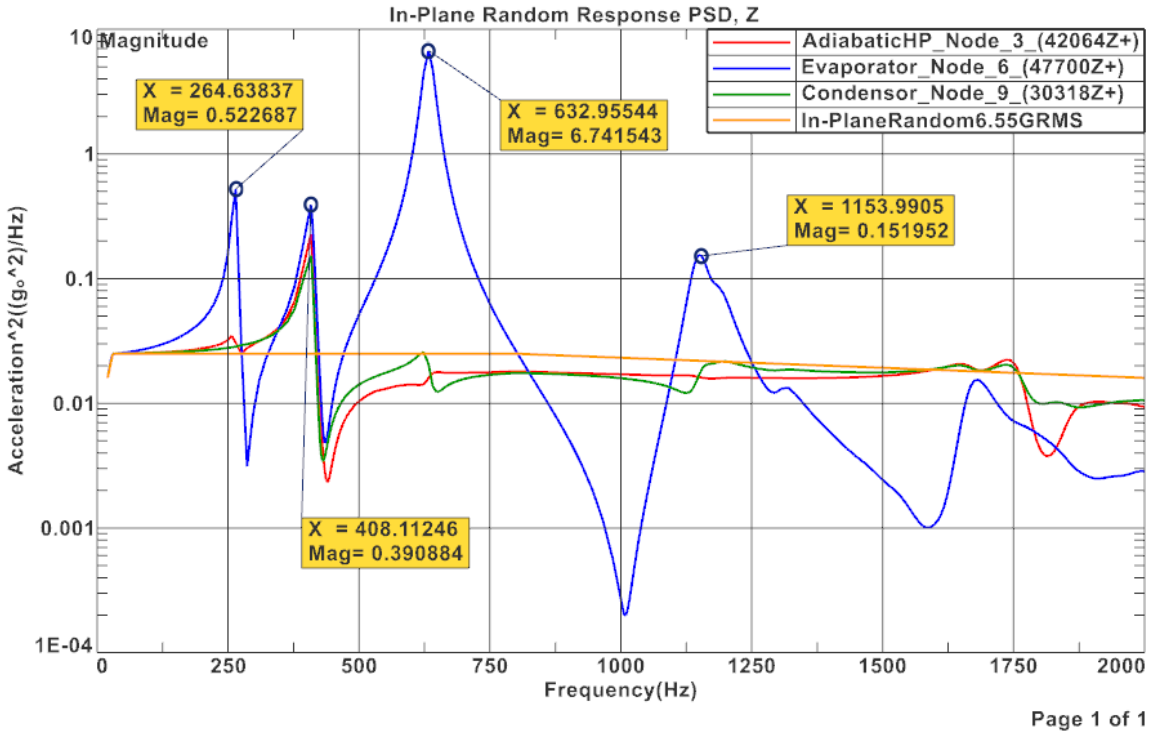

Fig 3.10. Response Curves from In-plane Random Response, Z

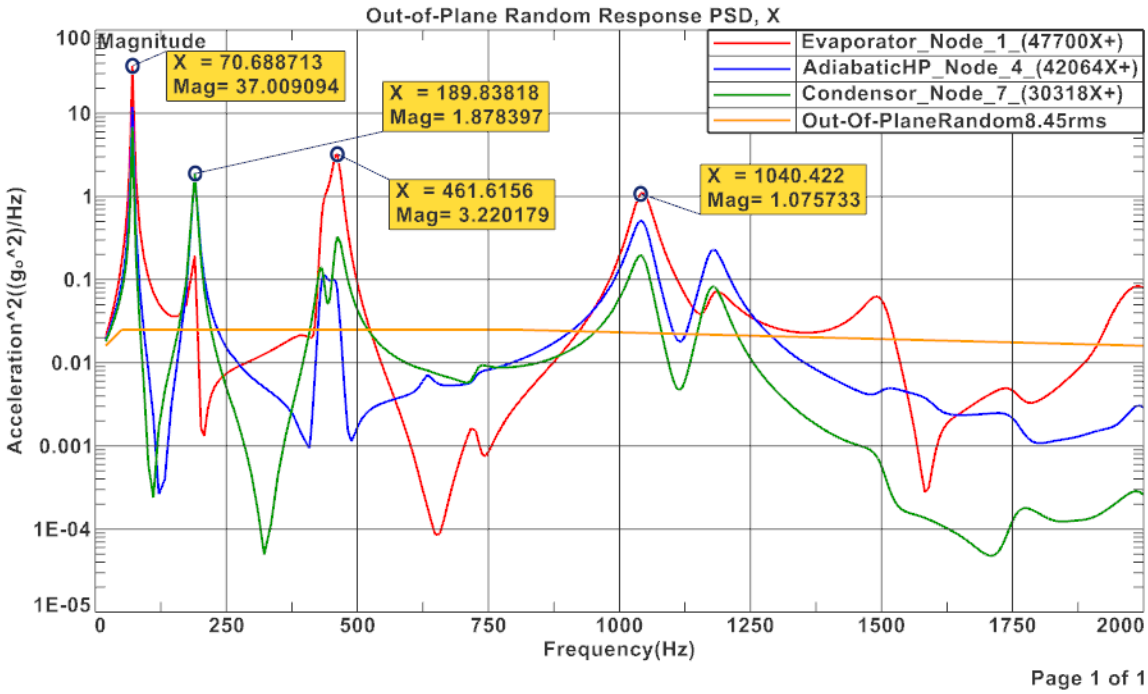

Fig 3.11. Response Curves from Out-of-plane Random Response, X

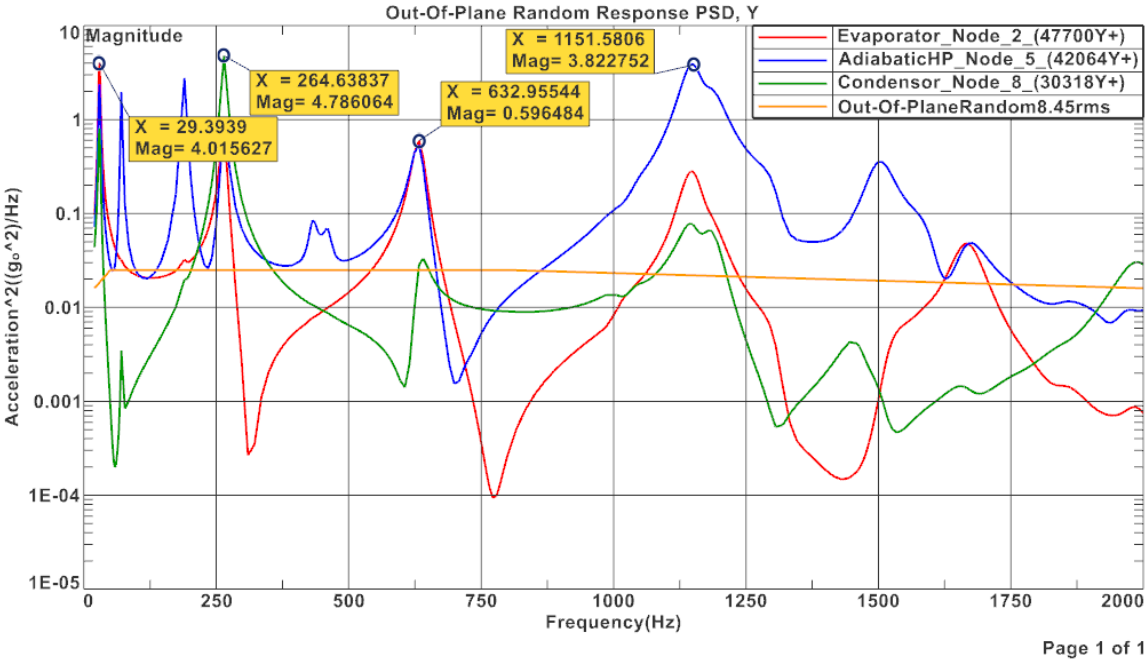

Fig 3.12. Response Curves from Out-of-plane Random Response, Y

Figures 3.10-3.12 above show the PSD response curves at the accelerometer locations and the random vibe signal pushed through the structure, seen in orange. As expected, we see a small response in the in-plane Z-direction and more significant responses in the out-of-plane X and Y-directions with respect to the natural modes of the structure. There is, however, a large PSD response in the In-plane direction at the 632.9 Hz frequency, which, as mentioned previously, is where we see the largest displacement in the evaporator section of the heat pipe. Therefore, the sine sweep response curves are valid as the large responses occur in expected locations. And will be used to evaluate the elemental high point stresses in the structure's heat pipe section. In addition, the random vibration PSD responses will be used to find the RMS von-mises stress concentrations on the heat pipe section of the structure. Both will carry three-sigma loads when calculating the equivalent yield factor of safety, FoS, of the heat pipe structure under load. Tabulated results for the sine sweep response and random responses are below in Table 3.6.

Table 3.6. Largest Sine Sweep Response Values

In-plane Sine Vibration Test Responses	
Frequency (Hz), Axes	Magnitude (g's)
-	-
Out-of-plane Sine Vibration Test Responses	
Frequency (Hz), Axes	Magnitude (g's)
70.68 Hz, X (Evaporator Section)	92.8
23.9 Hz, Y (Evaporator Section)	155.12

Table 3.7. Largest Random Response PSD Values

In-plane Random Vibration Test Responses	
Frequency (Hz), Axes	Magnitude (g^2/Hz)
632.95 Hz, Z (Evaporator Section)	6.74

Out-of-plane Random Vibration Test Responses	
Frequency (Hz), Axes	Magnitude (g^2/Hz)
70.68 Hz, X (Condenser Section)	37
1151.58 Hz, X (Adiabatic Section)	3.8

3.3 STRESS EVALUATION

As mentioned in section 3.2, we will be using the acceleration response curves from the sine sweep and random vibration responses to find the von-mises stresses on the structure. Before starting this analysis, we must establish an assumption concerning the elements used to mesh the heat pipe structure. Given the complex geometric nature of the heat pipe, mainly the internal hollow vapor space region, the structure was meshed using triangular TET4 elements. However, triangular elements are not ideal for stress results as the in-finite corners can produce false points of high stress on the element's edges. As such, the average centroidal stress result on the elements is used instead of the nodal elemental stress result. The RMS von mises stresses from the random vibration sweep are in Figures 3.13 and 3.14.

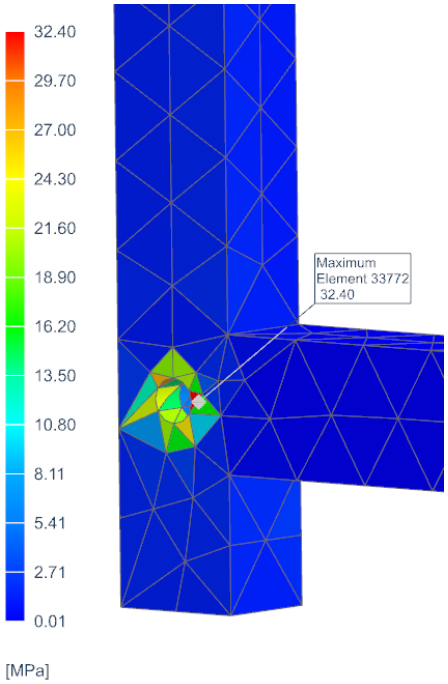

Fig 3.13. Max Stress from In-plane Random Vibration Sweep

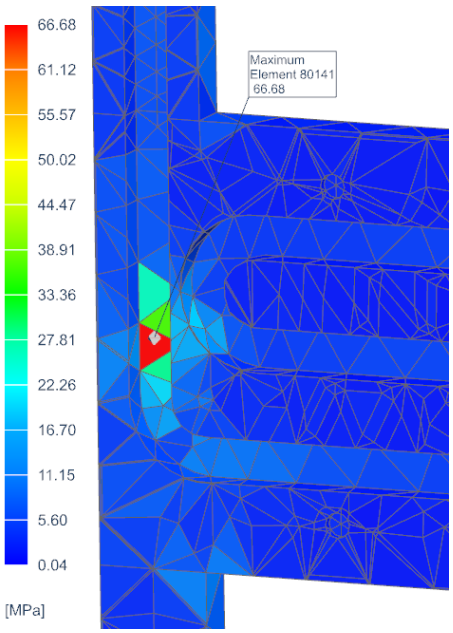

Fig 3.14. Max Stress from Out-of -Plane Random Vibration Sweep

Table 3.8. Max Stresses Random Response

In-plane Random Vibration Max Stress	
Location	Von-Mises Stress, MPA
Lower Bolted Region	32.4
Out-of-plane Random Vibration Max Stress	
Location	Von-Mises Stress, MPA
Inner wall, condenser	66.68

Taking the results from Table 3.8, we can find the yield factor of safety from the heat pipe structure under the random vibration load at three-sigma..

Table 3.9. Factors of Safety, Random Vibration Load

Random Vibration Von-Mises Max Stresses, Yield FoS				
	Stress, MPA	3σ, MPA	AlSi10Mg Yield, MPA	FoS
In-plane	32.4	97.2	230	2.37
Out-of-plane	58.17	174.5	230	1.31

The lowest yield FoS for the random vibration excitement occurs in the out-of-plane axis and has a value of 1.31. Therefore, we can assert that the 3D printed heat pipe structure is viable in the random vibration environment. Sine sweep stresses will be shown next in Figures 3.15 and 3.16.

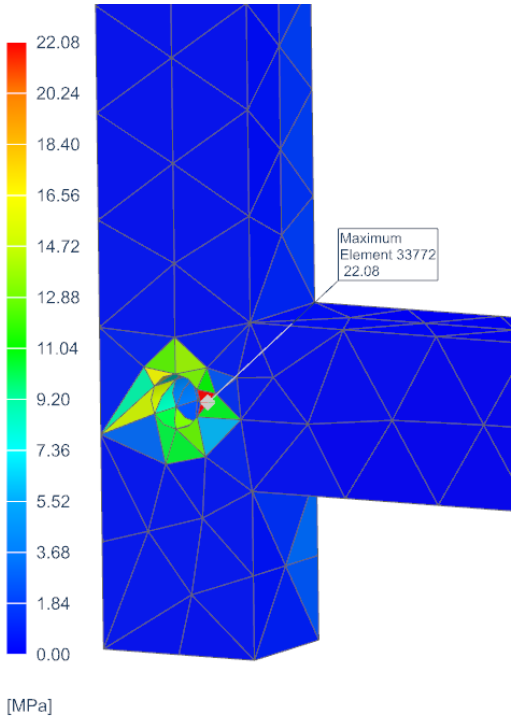

Fig 3.15. Max Stress from In-plane Sine Sweep

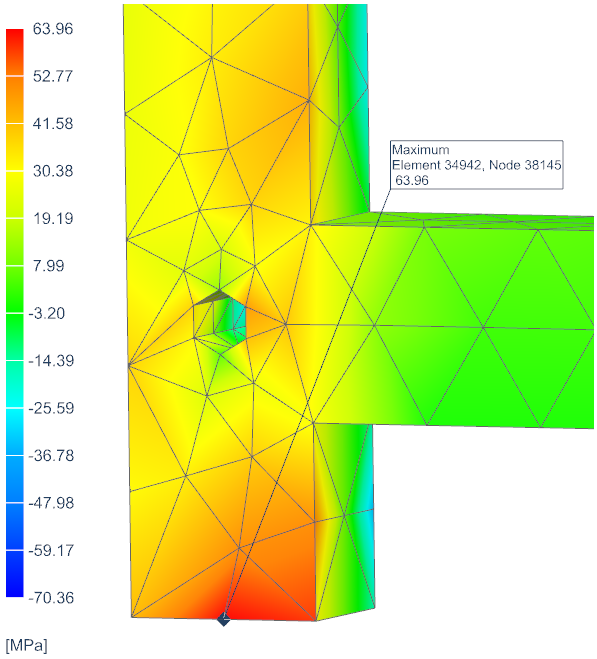

Fig 3.16. Max Stress from Out-of-plane Sine Sweep

Table 3.10. Max Stresses Sine Sweep Response

In-plane Random Vibration Max Stress	
Location	Von-Mises Stress, MPA
Lower Bolted Region	22.8
Out-of-plane Random Vibration Max Stress	
Location	Von-Mises Stress, MPA
Lower Bolted Region	63.98

Taking the results from Table 3.10, we can find the yield factor of safety from the heat pipe structure under the sine sweep load at three-sigma.

Table 3.11. Factors of Safety, Sine Sweep Load

Sine Sweep Von-Mises Max Stresses, Yield FoS				
	Stress, MPA	3σ, MPA	AlSi10Mg Yield, MPA	FoS
In-plane	22.8	68.4	230	3.36
Out-of-plane	63.98	191.94	230	1.20

The lowest FoS occurs in the out-of-plane axis with a value of 1.20 for the sine sweep response. Therefore, we can assert that the 3D printed heat pipe structure is viable in the sine sweep environment.

Before we move on from the structural analysis, taking a more detailed view of the region in the condenser section that experienced the largest stress in the out-of-plane

random response is worthwhile. This region was made up of TET4 elements of ~6mm size, and now we will look at the stress in the exact location with elements that are ~3mm in size. These results can be seen in Figure 3.17.

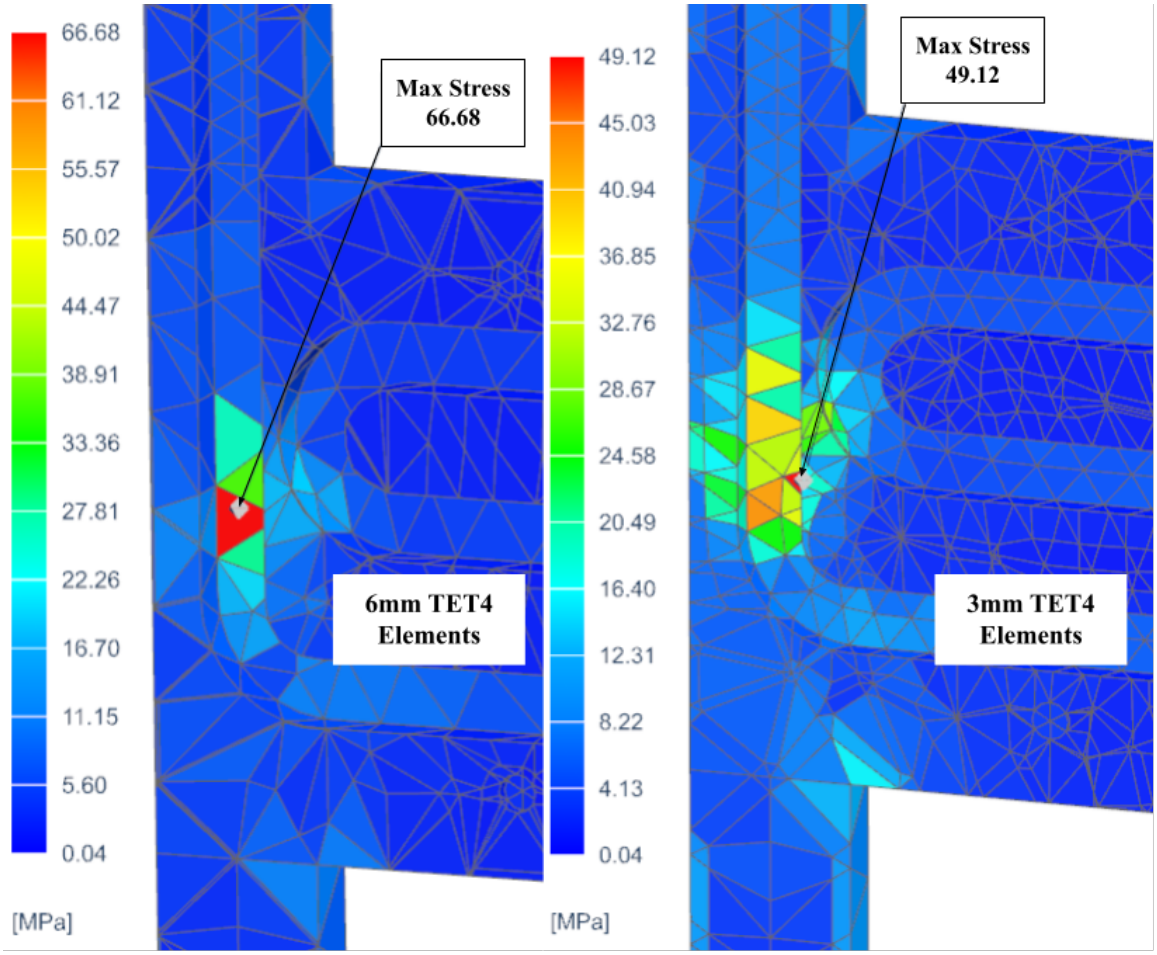

Fig 3.17. Sensitivity Study of Element Size

These smaller 3mm elements produced a max stress of 49.12 MPa compared to the 58.17 MPa seen with the original 6mm element size. The location of the max stress is near the same region and is still concentrated on a single element. If we look at the average stress of the elements directly surrounding the element of max stress, the 6mm elements have

an average stress of 39.24 MPa, and the 3mm elements have an average stress of 37.17 MPa. This is a difference of 2.07 MPa or 5.27%. We can conclude that the smaller element size does not produce results that conflict with the element size used for the FoS analysis, as the average elemental stress of that region is within 5%. The larger stress seen with the 6mm elements could be an overestimate as the larger element size takes up more of the actual width of the heat pipe section with only one element fitting across it, and the 3mm element can fit two complete elements in the same width of the heat pipe section.

CHAPTER 4: TECHNOLOGY IMPACT

The technology application studied here directly connects to the 2020 NASA Technology Taxonomy, which provides a structure for articulating the technology development disciplines needed to enable future space missions [19]. TX 14.2.2 Heat Transport directly calls for the advancement of heat transport technologies, including heat pipes, specifically in the area of increasing heat transfer efficiency. The topic addressed here shows the potential capability of raising the passive thermal management of up to 28W on the 3U CubeSat platform using additively manufactured heat pipes embedded into the structures of CubeSat busses. This enhanced heat dissipation capability can enable powerful in-flight computing and data analysis that may be currently infeasible in 3U CubeSat format. It is also important to note that much work has already gone into the field of 3D printed heat pipes for use on SmallSat platforms. Specifically, Advanced Cooling Technologies, Inc., with parts of their work being completed through NASA SBIR (small business innovation research) contracts, further shows the need for this

technology in the heat management space. ACT studied and tested a similar DMLS approach but instead of grooved heat pipes used a porous wicking structure in the manufacturing of their looped heat pipes [20]. ACT showed a maximum power of 125W in their study and was able to do this in 316LSS [20]. With the novel heat pipe structure studied here being closely aligned with the current technology needs of NASA, it is important to define the current technology readiness level at 3, with the ability to raise to 4 with the optimization of printing techniques in DMLS and subsequent benchtop testing.

CHAPTER 5: CONCLUSIONS

From the thermal and structural analysis conducted in this study, the conclusion can be drawn that a 3D printed heat pipe structure can be used as a novel approach to increase the thermal management capabilities in the 3U CubeSat platform while still maintaining structural viability in the launch load environment. The novel heat pipe structure can increase the platform's thermal management capabilities from a nominal power density of 4.7×10^3 W/m^3 to an order of magnitude larger of 1.0×10^4 W/m^3. This represents an internal heat load increase from 14W to 28W, doubling thermal load capabilities. This extra power load can represent the addition of high-power components that could not be effectively managed prior with heritage passive thermal management techniques. These high-power components can directly increase the technology capabilities of the SmallSat platform in the form of autonomy, science capability, onboard computing, detector sensitivity, etc. This study also showed that at three-sigma loads experienced in a standard rocket launch environment, the lowest factor of safety seen is 1.20, again assuming worst conditions and artificially increased von-mises stress

concentrations from using TET4 elements. 3D printing allows this heat pipe structure to be modified to accommodate a broad range of configurations, such as placing the evaporator directly on the high-power component to reduce the thermal resistance path to the evaporator. The evaporator can be placed anywhere within a 414.37 cm^3 volume within the CubeSat, shown in yellow in figure 4.1, making up roughly 1.5U's of configurable placement volume.

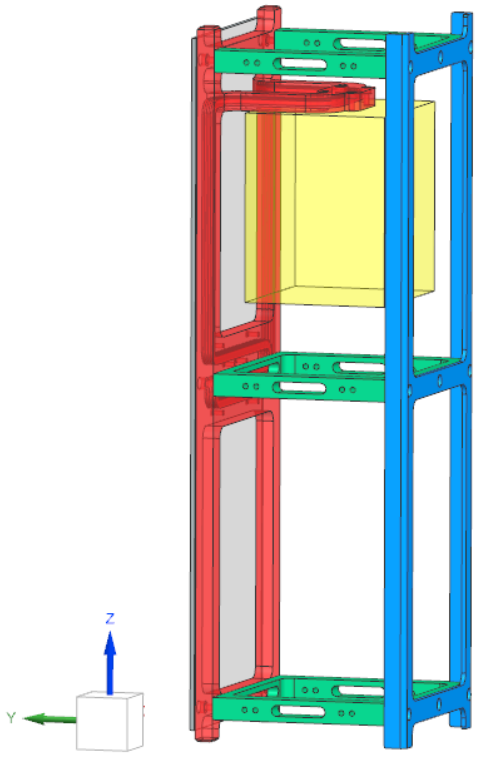

Fig 4.1. Bounding Box for Heat Pipe Evaporator Placement

Reducing the length of the adiabatic section can reduce the performance of the heat pipe, which is shown to be within a range of 44,853 W/mK to 77,184 W/mK, where this analysis used a nominal heat pipe effective thermal conductivity of 66,711 W/mK. The

actual internal volume of the novel heat pipe structure is only 8.3cm^3 since the adiabatic and condenser sections are built into the CubeSat structure. If the entire heat pipe system, including the evaporator, adiabatic, and condenser sections, were not built into the structure and had to be placed in the internal CubeSat structure, they would take up 48.7cm^3 of volume. This is an 82.9% reduction in internal volume need that other CubeSat systems can use. The other takeaway here is the method used to simulate the heat pipe in the thermal analysis. It is sometimes erroneously assumed that the entire heat pipe structure has the large thermal conductivity. The reality is that the vapor region alone has the large thermal conductivity, and the wicking structure and solid heat pipe structure are low thermal conductivity based on their material properties. Here the vapor space was modeled separately from the heat pipe structure, given the effective heat pipe thermal conductivity, and then tied to the solid heat pipe structure with a perfect contactor. This resulted in a 10.8% difference from the analytical calculation or a difference of 0.54^{o}C when placed under thermal load with a thermal sink on the condenser section.

The next phase would be refining the heat pipe structure to optimize it for 3D printing. One of the issues that would need to be addressed is removing the entire void inner cavity as the internal support material cannot be removed. This can be remedied by incorporating slots or plugs in the adiabatic and condenser sections that would allow for support material to be removed, Figure 4.2.

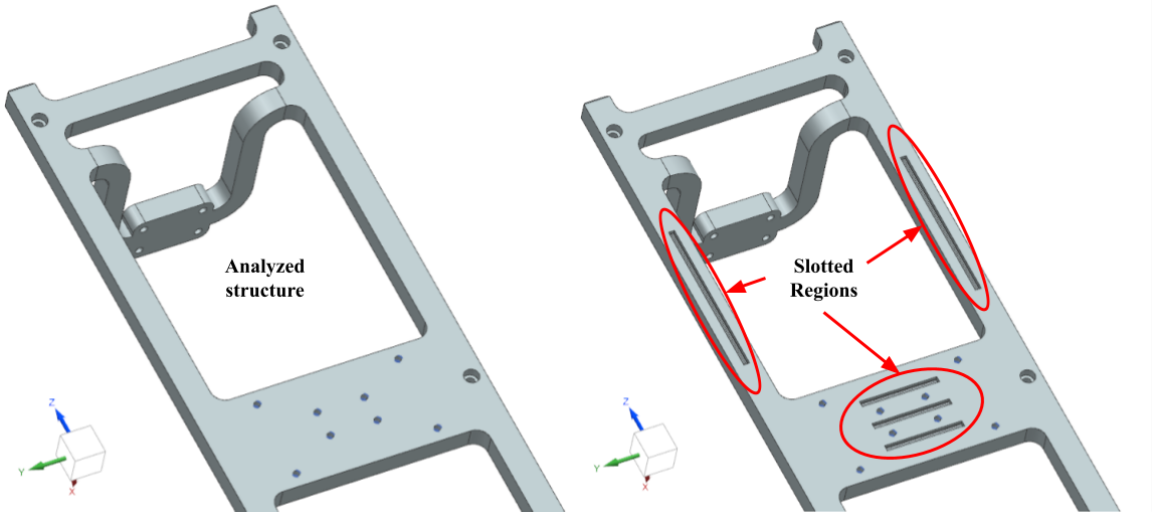

Fig 4.2. Potential Printing Configuration

After the print is complete, the holes left behind can be plugged with separately printed sections that can be welded on. Research has gone into the laser welding of AlSi10Mg, and the welded regions have shown an average strength of 163 MPa [18], a pressure not seen on the adiabatic or condenser sections in the structural analysis conducted here. Another modification would be adding a region that will allow for the vacuum filling and sealing of a working fluid to validate the verified results shown here with testing.

REFERENCES

[1] Arnold, S. S., Nuzzaci, R., & Gordon-Ross, A. (2012). Energy budgeting for CubeSats with an integrated FPGA. 2012 IEEE Aerospace Conference. https://doi.org/10.1109/aero.2012.6187240

[2] Brouwer, H., de Groot, Z., Jan van Gerner, H., & Guo, J. (n.d.). Solving the thermal challenge in power-dense CubeSats with water heat pipes. Retrieved June 27, 2022, from https://digitalcommons.usu.edu/cgi/viewcontent.cgi?article=3801&context=smallsat

[3] Chang, C., Han, Z., He, X., Wang, Z., & Ji, Y. (2021). 3D printed aluminum flat heat pipes with micro grooves for efficient thermal management of high power leds. Scientific Reports, 11(1). https://doi.org/10.1038/s41598-021-87798-4

[4] DEVERALL, J. E., SALMI, E. W., & KNAPP, R. J. (1967). Heat-pipe performance in a zero gravity field. Journal of Spacecraft and Rockets, 4(11), 1556–1557. https://doi.org/10.2514/3.29131

[5] Eos aluminium AlSi10Mg - Fathom. (n.d.). Retrieved June 27, 2022, from https://fathommfg.com/wp-content/uploads/2020/11/EOS_Aluminium_AlSi10Mg_en.pdf

[6] Gilmore, D. G., & Donabedian, M. (2003). Spacecraft Thermal Control Handbook. American Institute of Aeronautics and Astronautics.

[7] Heat Pipe Technology. Boyd Corporation. (n.d.). Retrieved June 27, 2022, from https://www.boydcorp.com/resources/temperature-control/heat-pipe-technology.html

[8] Kulu, E. (n.d.). Nanosats database. Nanosats Database. Retrieved June 27, 2022, from https://www.nanosats.eu/

[9] Metal 3D printing service for custom parts: Online quoting. Protolabs. (n.d.). Retrieved June 27, 2022, from https://www.protolabs.com/services/3d-printing/direct-metal-laser-sintering/

[10] Meyer, G. (2016). Design Considerations When Using Heat Pipes. Electronics Cooling, 36–41.

[11] Mäkikangas, J., Rautio, T., Mustakangas, A., & Mäntyjärvi, K. (2019). Laser welding of alsi10mg aluminium-based alloy produced by Selective Laser Melting (SLM). Procedia Manufacturing, 36, 88–94. https://doi.org/10.1016/j.promfg.2019.08.013

[12] Marc. (2019, December 1). *Heat Pipe Archives*. Celsia. Retrieved July 5, 2022, from https://celsiainc.com/heat-sink-blog/category/celsia-heat-pipe/

[13] NASA Technology taxonomy lowres. (n.d.). Retrieved June 27, 2022, from https://www.nasa.gov/sites/default/files/atoms/files/2020_nasa_technology_taxonomy_lowres.pdf

[14] Phoenix: A cubesat mission to study the impact of urban heat islands ... (n.d.). Retrieved June 27, 2022, from https://phxcubesat.asu.edu/sites/default/files/general/ssc20_asu_phoenix_cubesat_0.pdf

[15] Prasher, R. S. (2003). A simplified conduction based modeling scheme for design sensitivity study of thermal solution utilizing heat pipe and Vapor Chamber Technology. Journal of Electronic Packaging, 125(3), 378–385. https://doi.org/10.1115/1.1602479

[16] Richard, B., Anderson, B., Chen, C.-H., Crawner, J., & Augustine, M. (2019). Development of a 3D Printed Loop Heat Pipe. https://doi.org/ICES-2019-190

[17] Shah, H., & Gaywala, K. (2015). Design, fabrication & analysis of heat pipe for methanol, ethanol ... Retrieved June 27, 2022, from https://www.researchgate.net/publication/311887804_Design_fabrication_analysis_of_heat_pipe_for_methanol_ethanol_acetone_as_a_working_fluid

[18] Small satellite spacecraft providers. AAC Clyde Space. (2022, April 21). Retrieved June 27, 2022, from https://www.aac-clyde.space/

[19] Thermophysical properties: Acetone. ThermalFluidsPedia RSS. (n.d.). Retrieved June 27, 2022, from http://thermalfluidscentral.org/encyclopedia/index.php/Thermophysical_Properties:_Acetone

[20] Thermophysical properties: Methanol. ThermalFluidsPedia RSS. (n.d.). Retrieved June 27, 2022, fromhttp://www.thermalfluidscentral.thermalfluidscentral.org/encyclopedia/index.php/Thermophysical_Properties:_Methanol